

Dynamical and Surface Impacts of the January 2021 Sudden Stratospheric Warming in Novel Aeolus Wind Observations, **MLS** and ERA5

Corwin J. Wright¹, Richard J. Hall², Timothy P. Banyard¹, Neil P. Hindley¹, Isabell Krisch³, Daniel M. Mitchell², and William J. M. Seviour^{4,5}

¹Centre for Space, Atmospheric and Oceanic Science, University of Bath, UK

²School of Geographical Sciences and Cabot Institute for the Environment, University of Bristol, UK

³German Aerospace Center (DLR), Oberpfaffenhofen, Germany

⁴College of Engineering, Mathematics and Physical Sciences, University of Exeter, UK

⁵Global Systems Institute, University of Exeter, UK

Correspondence: Corwin Wright (c.wright@bath.ac.uk)

Abstract. Major sudden stratospheric warmings (SSWs) are extreme dynamical events where the usual strong westerly winds of the stratospheric polar vortex temporarily weaken or reverse and polar stratospheric temperatures rise by tens of Kelvin over just a few days, and remain so for an extended period. Via dynamical modification of the atmosphere below them, SSWs are believed to be a key contributor to extreme winter weather events at the surface over the following weeks. ~~Due to the major technical challenges involved in measuring wind from space,~~ SSW-induced changes to the wind structure of the polar vortex have ~~never previously been directly observed at the global scale~~ previously been studied in models and reanalyses and in localised measurements such as radiosondes and radars, but have not previously been directly and systematically observed on a global scale due to the major technical challenges involved in observing winds from space. Here, we exploit novel observations from ESA's flagship Aeolus wind-profiler mission, ~~supported by additional~~ together with temperature and geopotential height data from NASA's ~~MLS limb sounder and~~ Microwave Limb Sounder and surface variables from the ERA5 reanalysis, to study the 2021 SSW. This allows us to directly examine wind and related dynamical changes associated with the January 2021 major SSW, ~~the first such event in the Aeolus data record~~. Aeolus is the first satellite mission to systematically and directly acquire profiles of wind, and therefore our results represent the first direct measurements of SSW-induced wind changes at the global scale. We see a complete reversal of the zonal winds in the lower-middle stratosphere, with reversed winds in some geographic regions reaching down to the bottom 2 km of the atmosphere. These altered winds are associated with major changes to surface temperature patterns, and in particular we see a strong potential linkage from the SSW to extreme winter-weather outbreaks in Greece and Texas during late January and early February. Our results 1) demonstrate the benefits of wind-profiling satellites such as Aeolus in terms of both their direct measurement capability and use in supporting ~~reanalysis-driven~~ reanalysis-driven interpretation of stratosphere-troposphere coupling signatures, 2) provide a detailed dynamical description of a major weather event, and 3) have implications for the development of Earth-System models capable of accurately forecasting extreme winter weather.

1 Introduction

Sudden stratospheric warmings (SSWs) are some of the most dramatic dynamical events in the entire atmospheric system. Over just a few days, temperatures in the winter polar stratosphere can rise by as much as 50 K, while the circumpolar wind jet which usually separates the cold polar ~~stratospheric vortex from the wider atmosphere~~ stratosphere from midlatitudes dramatically reduces in speed and, at many heights and locations, can even reverse. These dynamical changes have major effects on both weather and longer-scale atmospheric processes: in addition to direct local changes to polar ozone and other chemistry (~~Tao et al., 2015; Safieddine et al., 2020~~) (Tao et al., 2015; Manney et al., 2015b, a; Safieddine et al., 2020), the altered wind patterns couple outwards to the broader atmospheric system with significant and widespread ramifications (Pedatella et al., 2018). In particular, SSWs ~~often act as the trigger for~~ can trigger extreme winter weather events at ground level in the heavily-populated midlatitude regions of North America and Europe, with significant social, safety and economic impacts (Kretschmer et al., 2018; Charlton-Perez et al., 2020; Hall et al., 2020).

The collapse of the circumpolar wind jet is arguably the most important factor affecting how SSWs interact with the broader Earth system. Reflecting this importance, the most broadly-used definition of a major SSW is wind- rather than temperature-based: specifically, a major SSW is ~~usually often~~ defined as a wintertime event in which the zonal mean at 60° and 10 hPa reaches zero (Charlton and Polvani, 2007). However, direct observations of the vortex winds are extremely technically challenging to make. While wind speed measurements using in-situ radiosondes and ground-based remote-sensing techniques such as lidar and radar are routinely made at many sites, the point-based nature of these techniques inherently limits their ability to characterise the large-scale changes SSWs induce in wind patterns.

Due to these observational limitations, the vast majority of recent research on how SSWs affect winds above the very bottom of the atmosphere has been carried out using models, reanalyses and winds inferred from gradients in other measured variables such as temperature. While these tools have proven highly effective and have significantly advanced our ability to predict winter weather around SSW events, they are not true measurements of wind speed — instead, they infer the wind state through a combination of numerical computation and/or how the wind affects and is affected by other atmospheric parameters.

Here, we exploit data from the European Space Agency (ESA)'s flagship Aeolus satellite mission to directly measure SSW effects on winds in the lower-stratospheric vortex for the first time. Launched in mid-2018, Aeolus is the first satellite instrument capable of systematically and directly measuring winds in the global free troposphere and lower stratosphere, and as such provides a unique window on how SSWs affect winds throughout the lower and lower-middle atmosphere. While Aeolus does not routinely measure winds as high as the 10 hPa (~32 km) level typically used to diagnose the presence of a major SSW, measurements are available from the surface to ~24 km (30 hPa). This height range allows us to study both a large fraction of the direct polar vortical changes induced by SSWs and also examine how these changes affect winds at all heights below.

~~We support and contextualise these Aeolus data with~~ In the atmosphere, in addition to Aeolus data we also use temperature observations and geostrophic wind estimates inferred from the Microwave Limb Sounder on NASA's Aura satellite and ~~with~~ wind, temperature and geopotential height (GPH) output from the European Centre for Medium-Range Weather Forecasts'

55 ERA5 reanalysis. We also investigate the potential surface impacts of the SSW, using temperature ~~and GPH data from ERA5~~
and, snow cover extent data from NOAA. We and GPH data from ERA5.

We first describe the Aeolus, MLS and ERA5 data in detail in Section 2; ~~the snow cover extent data are only used briefly~~
~~in this study and are described more fully by Robinson et al. (2014). In addition, Appendix A describes and justifies the~~
~~geometric adjustments we make to the Aeolus observations to produce the projected zonal and meridional wind products~~
60 ~~we use throughout this study.~~

~~We use these data to study the major SSW of early January 2021. This was the first and, to date, only SSW to occur~~
~~during standard Aeolus operations¹. Hence, we have designed our study to address the twin objectives of (1) characterising~~
~~SSW-induced dynamical changes for this event using novel observational data and (2) assessing the suitability of Aeolus data~~
~~for studying future extreme weather events of this type. We address these objectives in parallel throughout the study, rather~~
65 ~~than taking a series approach, in order to provide a clear narrative based around the physics of the event.~~

~~We first.~~ We next place the January 2021 SSW in its broader climatological context in Section 3, using ERA5 and MLS
data for all winters since MLS launched in 2004. Section 4 then describes the evolution of the 2021 event specifically using
zonal-mean Aeolus and MLS observations. We follow this with a brief discussion of the nature of the event in terms of vortex
summary metrics in Section 5, ~~and a more detailed analysis of mesoscale eddy forcing around the SSW period in Section ??.~~
70 ~~We then examine structural changes to the vortex at a~~ before moving on to examine sub-zonal level variability in Section 6, both
in terms of Aeolus wind ~~measurements (Section ??) and ERA5 GPH output (Section ??)~~ and MLS GPH measurements. Finally,
in Section 7 we study ~~possible surface impacts of the event~~ surface weather impacts associated with the SSW temporally, before
discussing our results and drawing conclusions in Section 8.

2 Data

75 2.1 Aeolus

Aeolus is ESA's fifth Earth Explorer mission (~~Stoffelen et al., 2005; ESA, 2008; Reitebueh, 2012~~) (Stoffelen et al., 2005; ESA, 2008; Reitel
, which launched in mid-2018. The Aeolus satellite itself is a polar orbiter, in a 320 km sun-synchronous dawn-dusk 97° incli-
nation orbit with equator-crossing local solar times of 06:00 and 18:00 in the descending and ascending node respectively. This
orbit approaches each pole 15.6 times per day, and thus provides a platform well-suited to characterising polar atmospheric
80 dynamics.

The satellite carries a single primary payload, the Atmospheric Laser Doppler Instrument (~~ALADIN; Chanin et al., 1989; ESA, 1989~~)
. This is a Doppler wind lidar designed to measure winds, aerosol and cloud in the bottom 30 km of the atmosphere. A
335 nm laser directed at 35° off-nadir and 90° off-track measures both molecular (Rayleigh) and aerosol (Mie) backscatter.
We use baseline-12 Rayleigh data, which has a vertical resolution ~ 0.5 –1–2 km depending on scanning mode and a horizontal
85 (along-track) resolution of ~ 90 km for the profiles studied. Following corrections for hot pixels, telescope-temperature-dependent

¹ ~~A major SSW occurred a few months after launch in January 2019, but this was during an early phase of instrument operations for which data are not reliable.~~

biases and a longitude-dependent bias, a mean instrument bias $\lesssim 0.6 \text{ ms}^{-1}$ has been estimated for these data relative to northern-midlatitude radiosondes and to NWP models (Rennie and Isaksen, 2020; Martin et al., 2021). (Chanin et al., 1989; Weiler et al., 2020; Rennie et al., 2021). For quality control, we require that the HLOS error estimate set by the retrieval is $< 8 \text{ ms}^{-1}$ and that the data are not cloud-contaminated (i.e. Rayleigh-clear only).

90 Aeolus measures horizontal line-of-sight (HLOS) winds relative to the lidar boresight¹. However, atmospheric dynamics is usually described in a resolved zonal/meridional framework, and thus we convert our observations into this frame. Appendix A describes this conversion and estimates errors arising from it, concluding that in our study region (i) zonal winds are generally robust except at the very highest latitudes, but (ii) meridional winds are only useful when heavily averaged, and even then have significantly suppressed magnitudes, typically by a factor of about ten. Except in Appendix A, we generally refer to our projected zonal and meridional wind estimates in this study without qualifying that they are derived in this way, but this distinction is important and should be kept in mind. In particular, in several places in this study we scale Aeolus estimates of v by this empirically determined factor of 10; while we highlight this scaling in every case and treat the results sceptically, the true difference between Aeolus and real v is likely to vary both spatially and temporally and any such scaling is at best an approximation. the underlying assumptions we make to carry it out.

100 Additionally, Aeolus' vertical scan pattern changes regularly. While the instrument is capable of measuring wind speeds at heights up to 30 km, in practice the height-spacing-height range and spacing of individual profiles varies to accommodate both specific science objectives and a broader numerical weather prediction role. We regularly grid our data for analysis to remove the effects of irregular vertical spacing, but we cannot compensate for the varying maximum measurement altitude; as such, As operated at time of data collection for this study, the maximum height level of our study varies significantly, typically between heights of 17–25 km. maximum altitude of the Aeolus wind dataset was typically lower equatorward of 60°N than it was poleward. This is illustrated by Figure 1b, which shows the spacing in height and latitude of Aeolus measurements for the first complete orbit on the 5th of January 2021 poleward of 50°N ; this orbit is broadly typical of the study period from mid-November onwards. As such, to provide a uniform spatial average for all comparisons, throughout this study we average over the region $60\text{--}65^\circ\text{N}$ in all analyses intended to characterise atmospheric dynamics and structure around 60°N , to ensure a fair comparison at all heights.

2.2 Microwave Limb Sounder

We use v5.0 Level 2 data from the Microwave Limb Sounder on NASA's Aura satellite. Launched in 2004, Aura flies in a sun-synchronous polar orbit with equator-crossing times of 01.30 and 13.30. MLS uses a limb-sounding technique to measure atmospheric microwave emissions in five spectral bands (Schoeberl et al., 2006; Waters et al., 2006)(?). Temperature and pressure are obtained from the 118 and 239 GHz bands, retrieved over the range 261—0.001 hPa ($\sim 10\text{--}100$ km). Vertical resolution is variable, monotonically improving from 5 km – 3.6 km over the height range 10-25 km before monotonically worsening again to 5 km at 40 km (see e.g. Figure 6a of Wright et al., 2016); (see Figure 1b for sampling and e.g. Figure 6a of

¹A small vertical wind w component is present in the output HLOS data, causing an error $\sim 1.32w$. As w is usually small relative to u and v except in extreme cases such as strong gravity wave activity, we assume the standard Aeolus HLOS retrieval assumes this effect to be negligible.

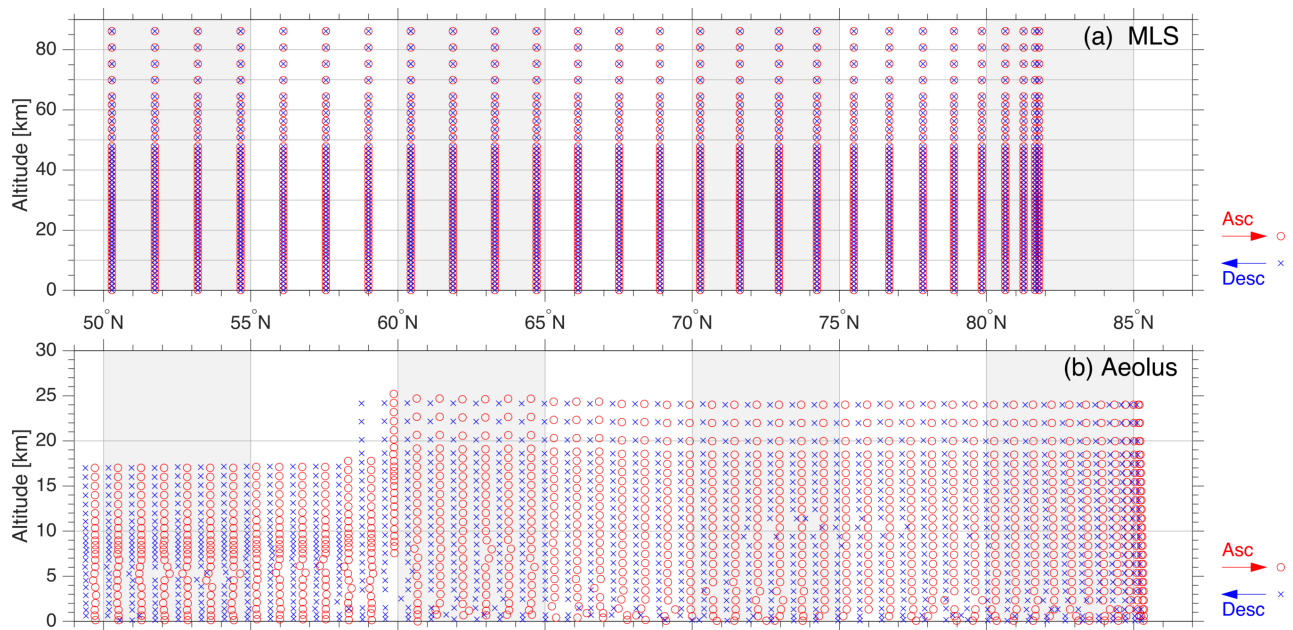


Figure 1. Illustration of (a) MLS (b) Aeolus measurement spacing in northern polar regions. On each panel, the first complete part-orbit crossing poleward of 60°N on the 5th of January 2021 is shown - this orbit is typical for those during our study. Red circles indicate measurements on the latitude-ascending node of the orbit and blue crosses measurements on the latitude-descending node of the orbit. Data are shown on their retrieval grids, which do not inherently correspond to the true resolution of the measurement. Note in particular the sharp change in height coverage at around 60°N in Aeolus data.

Wright et al. (2016) for resolution. This is finer than most nadir-sounding instruments, but significantly coarser than Aeolus. Along-track In the UTLS, along-track resolution is ~ 170 km, and estimated temperature precision is ~ 0.6 K in the UTLS (Livesey et al., 2015), and estimated temperature accuracy is -2.5 – $+1$ K (Livesey et al., 2015). Figure 1a shows the spacing of these measurements for a typical orbit.

We also derive geostrophic winds from MLS data. These winds are computed from the MLS v5.0 Level 2 GPH product, which is itself primarily derived use MLS geopotential heights (GPH) and geostrophic winds. The GPH product is retrieved from the 118 GHz and 234 GHz O₂ spectral bands (Livesey et al., 2015), using the methodology described by Schwartz et al. (2008), and primarily derives from MLS temperatures (Livesey et al., 2006). Our MLS winds are calculated In the height range studied, the product used has a vertical resolution of 4–12 km, a precision of 20–110 m, and an accuracy error of 0–150 m, with the less precise/poorer resolution extrema more typical of the top of the column.

We compute geostrophic winds from these GPH data, on a 5° × 20° latitude/longitude grid independently for each MLS pressure level and day, using. We use the relation $u = -(g/f)dZ/dy$, where Z is GPH, y is the meridional distance between measurement bins, f is the Coriolis parameter and g is the acceleration downwards due to gravity (assumed to be 9.81 ms^{-2}). Values estimated on this grid are then bilinearly interpolated back to the instrument scan track, again for each pressure level

and day independently, in order to provide a spatial weighting roughly equivalent to that for MLS temperature. This choice is made to provide better comparability between analyses produced using the temperature, GPH and wind datasets.

135 **Due to** this significant spatiotemporal averaging, these geostrophic winds are very coarse relative to Aeolus. The calculation also inherently relies on an assumption of atmospheric geostrophy. In our study region, we expect the difference between geostrophic and true wind to increase with height **due to** the driving effects of processes such as gravity wave breaking, and MLS wind estimates at high altitudes in particular should be treated with caution. We use only zonal-mean zonal MLS wind in this study, which we validate against Aeolus, reanalysis and operational analysis zonal-mean zonal winds in the troposphere and stratosphere in Section 2.4.

140 MLS data are unavailable for a large fraction of the 24th of December 2020, and the remaining data collected data for this day exhibit a markedly different zonal mean and height dependence when compared to the surrounding days. **We believe that** this difference is due to the partial data coverage rather than true geophysical differences. Accordingly, to remove the effect of this anomalous day from our analyses, this day has been replaced in all analyses by the mean of the 23rd and 25th December 2020.

145 **2.3 ERA5 and ECMWF Operational Analyses**

We use ERA5 reanalysis output (Copernicus Climate Change Service, C3S; Hersbach et al., 2020) and European Centre for Medium-range Weather Forecasting (ECMWF) operational analysis (hereafter ‘OpAl’ for brevity). OpAl is only used in Section 2.4, where zonal-mean zonal wind is shown to be almost identical to ERA5 at the heights and times considered in the zonal mean, and in the rest of the study we use ERA5 only.

150 ERA5 is a fifth-generation reanalysis product produced by the ECMWF. OpAl is broadly similar in concept, but use a current version of the assimilative IFS weather model - for this study, IFS Cycle 47r1 - rather than a fixed version as with ERA5, which uses IFS Cycle 41r2, a 2016 version of the operational model. Furthermore, OpAl assimilates Aeolus data, while ERA5 does not. Therefore, ERA5 data are independent of Aeolus, while OpAl data are constrained by it. ERA5 is however constrained by other data sources, including in this altitude range by aircraft, radiosondes and satellite radiance and bending angle data, and
155 therefore should reflect broadly the same geophysical state.

We use several forms of ERA5 data:

- In Figures 2 – 5, Figure ??, and Appendix A, we use temperature and zonal and meridional wind fields stored on 137 levels spaced non-uniformly from the surface to 0.01 hPa. These have been downsampled to a spatial resolution of 1.5° and to a 3 hour time resolution to facilitate analysis of comparatively large data volumes.
- 160 - In Figures 6, 9 and 10, 10 and 11 we use GPH stored on 37 pressure levels spaced non-uniformly from the surface to 1 hPa (~ 48 km altitude), with daily (specifically, midnight UTC) temporal resolution and at the full spatial resolution of 0.25° .
- In Figure 10 we use the daily snowfall field, also on a 0.25° grid.

– In Figures 10 and 11, we use the daily midnight 2 m altitude temperature field, also on a 0.25° grid.

165 Like all reanalyses and models, these datasets inherently exhibit meaningful differences from the observed atmospheric state, both systematic and random, particularly at short lengthscales and high altitudes. Although systematic assessments of high-altitude wind accuracy at the global scale are challenging to produce due to a lack of suitable observations and GPH is not a measurable quantity, an assessment of temperature relative to limb sounder data suggest that, at the altitudes considered here, pointwise differences from observations were generally small, with typical pointwise root-mean-square temperatures differences from limb sounder observations <2 K and Pearson linear correlations >0.95 (Wright and Hindley, 2018).

170 ERA5 data are only available for complete months ending at least two months before time of access. For periods closer to the date of access than this, an interim product known as ERA5T is made available at a five-day lag, which is produced in the same way as standard ERA5. This product is typically expected to exhibit no differences from the final product, but this is not guaranteed. Based on our date of article submission, we use ERA5T for all dates after the beginning of 2021, but due to the expected high level of similarity with the final ERA5 product refer to the two datasets interchangeably as ERA5. If this manuscript is accepted for WCD, we will replace these data with ERA5 during the revision process, highlighting any output changes at that time in our reviewer response and removing this paragraph.

2.4 Geostrophic Wind ~~Validation~~ Cross-Validation

Figure 2 shows time series of zonal mean zonal wind speed \bar{u} derived from Aeolus (blue), ERA5 (pink dashed), OpAl (red), and MLS (orange), all averaged over the 55° – 65° N latitude band and shown at the (Figure 2a) 32 km, (2b) 22 km and (2c) 15 km altitude levels. 32 km represents the usual level at which SSWs are defined, but is not measured by Aeolus; 22 km is the highest altitude measured by Aeolus for the great majority of the period studied (commencing in mid-November) and 15 km is the highest altitude level at which Aeolus measurements are made for the entire period studied (i.e. including early November). While this Figure shows clear evidence of the large dynamical changes due to the SSW that are the focus of our study, our primary ~~purpose aim~~ here is to ~~cross-validate~~ assess the consistency or otherwise of these four datasets, and we therefore reserve detailed discussion of the dynamical situation to Section 3 onwards. ~~Aeolus data are not available in the top height level, and only commence in mid-November in the middle level.~~

Very close agreement is seen between the four zonal mean time series, with Aeolus-relative correlations ≥ 0.98 ≥ 0.95 in all cases and root-mean-square-differences of ≤ 3.70 < 3.2 ms^{-1} . Good visual agreement is also seen between MLS and reanalysis/operational analysis in the 32 km data. Based on this comparison, we conclude that MLS \bar{u} is sufficiently robust in the zonal mean for use in our study, at least at these altitudes and latitudes; this reinforces the results of ~~the manney~~ previous studies that have used these data to understand SSW dynamics (e.g. Manney et al., 2008, 2009, 2015b) (e.g. Manney et al., 2008, 2009, 2015b; Smith et al. . We further conclude that ERA5 and OpAl data in the zonal mean are sufficiently similar that they can be used interchangeably for our purposes; since some later analyses involve comparisons to climatology, we therefore use ERA5 throughout the remainder of this study for consistency.

Some differences are seen between the datasets, but these differences are small - this is consistent with the high quality of the datasets and very large spatial averaging implicit in taking a zonal mean. ~~In particular, at the 22 km level both of the assimilative model datasets, i.e. ERA5 and OpAl, see \bar{u} passing below 0. Aeolus typically exhibits more positive values of u before and during and lower values of u after the SSW relative to the ECMWF products, while MLS has more positive u both before and after but more negative u during the SSW. At the 15 ms^{-1} a few days after the observational datasets. They also underestimate both local maxima and minima in \bar{u} during the period after this, including missing a brief reversal seen by Aeolus but not MLS~~ km level, Aeolus generally has more positive u than the ECMWF products except for brief periods, while MLS u is again more positive before the SSW and more negative during. Closer investigation of these ~~discrepancies~~ differences, including their geographic structure at spatial scales below the zonal mean, is beyond the scope of our study but may be a fruitful path for future work.

3 The Climatological Context of the 2021 SSW

~~While Aeolus launched in 2018 and was observing the atmosphere during winter 2018/19, due to laser instrument sensitivity issues and associated tests data products are only reliable from late June 2019 onwards. Furthermore, data for the 2019/20 winter remain unavailable due to reprocessing requirements. Therefore, we are only able to consider data from winter 2020/21 in this study. However, it is important to place this winter in context, in order to ascertain how representative our results are of winters in general and SSWs more specifically.~~

Figure 3 shows (a,c,e) MLS zonal mean temperature \bar{T} and (b,d,f,g) ERA5 \bar{u} , analysed relative to a climatology produced using all winters between 2004/05 and 2019/20, i.e. the period since MLS began collecting data. \bar{T} has been averaged across the entire region poleward of 60°N to provide an estimate of the mean polar context (but note that MLS data only extend to 82°N), while \bar{u} has been averaged zonally across the 55 ~~60~~ $^\circ\text{N}$ – 65°N latitude band to focus on the strength of ~~the vortex edge winds~~ winds in regions closer to the nominal edge of the polar vortex under undisturbed conditions.

~~Figure 3 shows~~ We show data at the (a,b) ~~2032~~ km, (c,d) ~~1522~~ km, (e,f) ~~1015~~ km and (g) 5 km levels for all polar winters; the first three have been selected for consistency with Figure 2, with the fourth added to provide tropospheric context. 2020/21 is shown in red. Grey shading illustrates the spread of the 2004/05–2018/19 climatology, with shades of grey indicating specific positions in the climatology and with the 0th, 18th, 50th, 82nd and 100th percentiles (i.e. non-parametric equivalents of the range, median, and first and second standard deviations) emphasised by solid grey lines. For a fifteen-winter climatology such as this, the regions above and below the 18th and 82nd percentiles respectively represent three individual winters each, while the region between these bounds represents the remaining nine winters. There have been two previous early-January major SSWs since 2004 (Butler et al., 2017), reaching zero \bar{u} at 10 hPa, 60°N on the 6th of January 2013 and 2nd of January 2019 respectively. ~~We therefore broadly expect a ‘typical’ SSW to fall somewhere above the 82nd percentile for temperature and below the 18th percentile for wind relative to this climatological period, but not to dramatically exceed the full range~~ As these previous SSWs contribute strongly to the relatively short climatological period shown, we therefore do not inherently expect

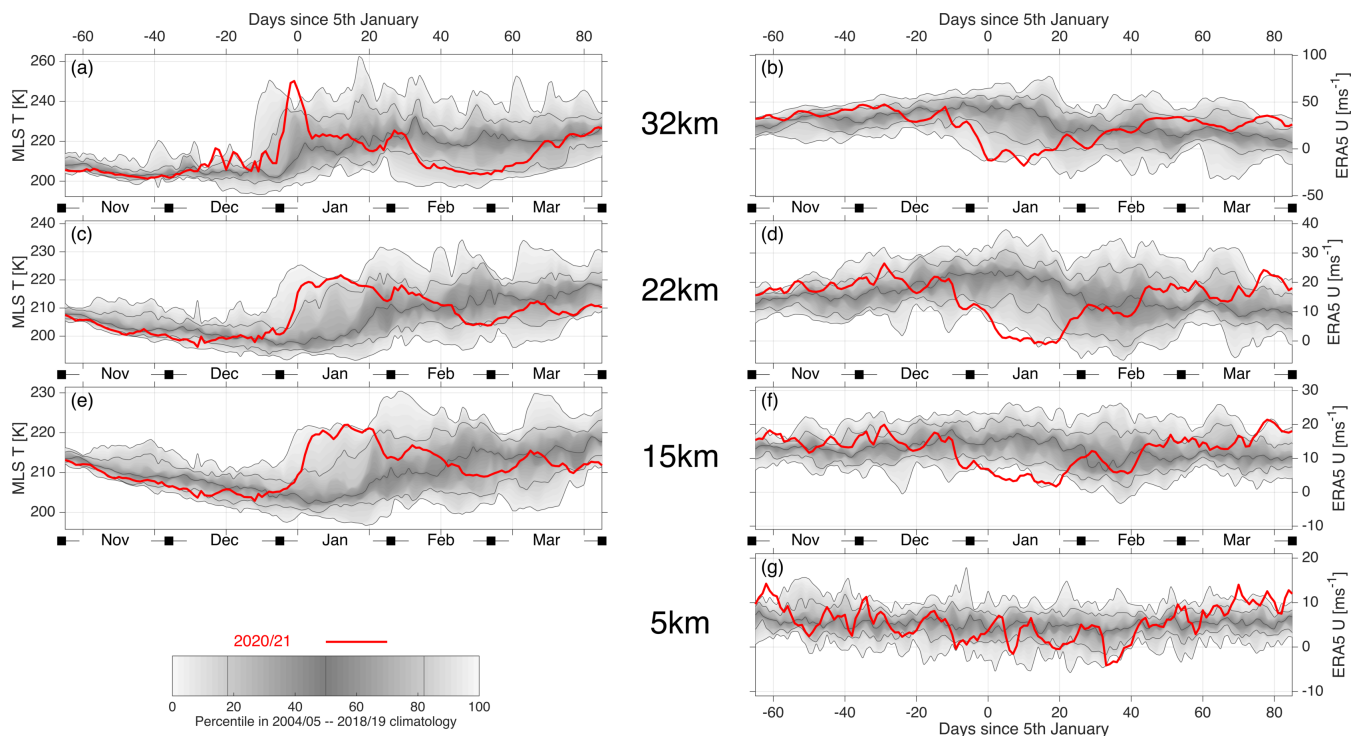


Figure 3. Context of the January 2021 SSW in relation to a 2004/05–2019/20 climatology of zonal mean (a,c,e) MLS temperatures and (b,d,f,g) ERA5 zonal winds at (a,b) 2032 km (c,d) 1522 km (e,g) 1015 km and (g) 5 km altitude. Grey shading shows the climatological distribution, with the 0th, 18th, 50th, 82nd and 100th percentiles (i.e. non-parametric equivalents of the range, median, and first and second standard deviations) emphasised by solid grey lines. Red line shows winter 2020/21 within this context.

the 2021 SSW to automatically exceed the shaded range, although given the heterogeneity of dynamical states and start dates within the observed record of SSWs it can do so.

230 \bar{T} before early December is below the central at or below the centre of the climatological range at the 2032 km and level and below it at the 22 km and 15 km level, rarely exceeding the 18th percentile. At the 10 km level, it lies in the central portion of the distribution, with a small excursion to a brief record minimum in mid-December levels, only rarely approaching the 50th percentile at the lower two heights. \bar{u} during this period at altitudes ≥ 15 km is significantly all altitudes is noticeably above climatology to a similar degree as \bar{T} is above; this is physically consistent, as it represents a strong vortex boundary which isolates the pole from midlatitudes and allows it to radiatively cool, suggesting that the polar vortex was anomalously strong in this period. \bar{u} below below > 15 km. \bar{u} at 5 km show no consistent trend during this period, varying for example from an all-climatology maximum in early November to a near-minimum two weeks later.

From early December to around the 1st of January at heights ≥ 15 km, \bar{T} starts to rise slightly, while \bar{u} drops significantly. Around the 1st of January, the rise in \bar{T} rapidly accelerates, moving from the centre of the climatological distribution to near-record climatology-topping values by the 5th of January and remaining at this level for around 18 days. \bar{u} during this period

reaches a ~~record-climatology-relative~~ minimum for this time period. After this maximum (minimum) in \bar{T} (\bar{u}), temperatures (winds) start to slowly return to ~~normal; this return to normality~~ is a mixture of falling temperatures during 2021 and a rise in the climatological median and range (~~albeit partly due to the presence of later SSWs in other years within the data record~~), and vice-versa for \bar{u} . After the first week of February, temperatures and winds at these altitudes remain within the central region
245 for the remainder of the study period.

At ~~altitudes ≤ 10 the 5 km~~, ~~temperatures rise above the 82nd percentile following the SSW, fall back below this percentile around 20 days later and remain near the centre of the distribution for the rest of the period.~~ ~~level,~~ \bar{u} at these heights shows no major response to the first minimum of the SSW in early January. A ~~local~~ minimum in \bar{u} is seen around day 35 of the year at the 5 km ~~level and 15 km levels~~, which may be associated with a second \bar{u} minimum associated with the SSW shown later in
250 our study (Figures 5 and 8).

~~In general therefore, we conclude that the 2020/21 SSW was broadly typical for an SSW in the period since (at least) 2004 in terms of zonal-mean effects on UTLS polar dynamics, with winds and temperatures at or near date-record values but not dramatically exceeding them.~~

4 Zonal-Mean Winds and Temperatures in the Winter 2020/21 Sudden Stratospheric Warming

255 Figures 4 and 5 show MLS- and Aeolus-derived \bar{u} and \bar{T} for winter 2020/21, again averaged over the region poleward of 60°N for temperatures and over the ~~55~~ 60° – 65°N latitude band for winds. Temperatures are shown as zonal mean anomalies \bar{T}_a from the the mission-to-date day-of-year median, ~~i.e., the difference between 2020/21 zonal-mean temperature and median climatological zonal-mean temperature~~; this is intended to both remove the strong vertical dependence of temperature on height and contextualise the data in the historical record. ~~Supplementary Figure S1 shows absolute measured temperatures on the same axes as Figures 4a and 5a for context.~~
260 ~~axes as Figures 4a and 5a for context.~~

For Aeolus \bar{u} (Figure 5b), the bottom few kilometres represent an incomplete zonal mean (for example, ~~Greenland~~ reaches maximal altitudes of >3 km in this latitude band) and a more technically challenging measurement than at higher altitudes. Thus, altitudes below 2 km have been omitted completely and altitudes below ~ 5 km should be treated with caution, although we note that case studies ~~and validation campaigns~~ using Aeolus data have shown plausible ~~and consistent~~ results at even the
265 lowest altitudes (~~e.g. Banyard et al., 2021~~)(e.g. Lux et al., 2020; ~~?~~; Banyard et al., 2021).

~~Times are shown as days relative to the 5th of January 2021. Aeolus data have been binned onto 2021 on the centre-figure axes and as dates on the outer-figure axes, with minor ticks indicating a step of one day. Aeolus data are shown at a 2 km by one-day grid resolution, as described in Appendix A.~~ For MLS, daily time bins are also used, but the width of the height bins is set to 4 km at altitudes below 55 km altitude and 6 km above. The green and purple dot-dashed lines overlaid on the data
270 shows the zonal-mean temperature-tropopause and -stratopause height at 60°N for that day, derived from ERA5 as described by Wright and Banyard (2020) and France et al. (2012) respectively. A wider latitude range (50°N – 70°N) was also tested for Aeolus winds; results were broadly similar but with a deeper and longer-lasting period of negative-zonal winds at the top of the measured column following the SSW.

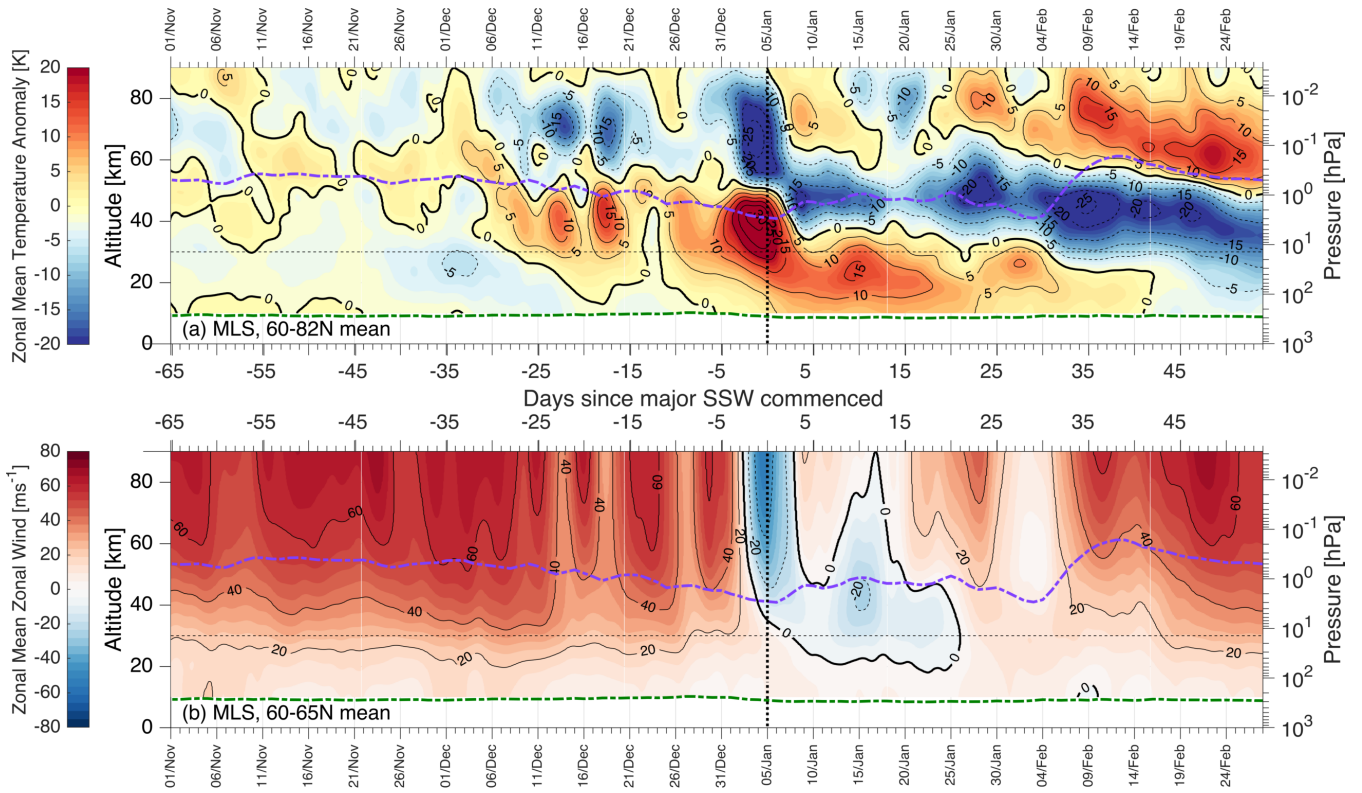


Figure 4. MLS-derived (a) 60°N–90°N mean temperature anomalies; (b) 55°N–65°N mean geostrophic zonal winds over the height range 0–90 km for winter 2020/21. Mean tropopause (stratopause) height derived from ERA5 is shown as a dot-dashed green (purple) line. Vertical dotted line indicates the date at which 10 hPa winds reversed and the SSW became defined as major. Horizontal dashed line indicates the top of Figure 5.

4.1 Stratospheric and Mesospheric Context

275 We consider first the broader-scale picture provided by Figure 4. Polar-cap temperature (Figure 4a) is typical for the around
the median for this time of year in November, with $|\overline{T_a}| < 5$ K at all heights. $\overline{T_a}$ is small and negative in the mid-stratosphere
and mid-mesosphere and small and positive around the stratopause and (in early November) in the upper mesosphere. The
small local maximum around the stratopause is likely due to interannual stratopause height variability rather than a meaningful
difference. Vortex-edge winds The zonal mean zonal wind at 60–65°N during this period (Figure 4b) during this period are
280 generally strong and zonal is generally large and positive throughout the stratosphere and mesosphere, but with a noticeable
dip in mid-November, particularly in the mid-mesosphere.

From around the 1st of December, mid-stratospheric $\overline{T_a}$ dips to more than 5 K below climatology for a few days, while
mesospheric $\overline{T_a}$ becomes anomalously positive up to above 80 km altitude. These signals, while small, mark the start of a
period of significant disruption at all heights, associated with a steady drop in stratopause height. Throughout early December,

285 stratospheric temperature is significantly above climatology, reaching short-lived peaks of $\overline{T_a} > 10$ K. In the mid-mesosphere, similar-magnitude negative anomalies are seen, with corresponding timing. \overline{u} during this period alternately speeds up and slows down by a significant fraction, with the timing of these changes well-correlated with the temperature changes (and with changes in tropospheric eddy heat flux $v'T'$, shown and discussed in Section ??). This variability is strongly associated with the vortex beginning to distort and break up (Section 6); these modulations may be related to the polar vortex vacillations which have been hypothesised to precede regime transitions from a strong to a weak vortex state (e.g. Scott, 2016).

290 From the 20th of December, $\overline{T_a}$ returns to normal for around five days at all heights, with $|\overline{T_a}| < 5$ K at all heights except for a small local maximum at the stratopause and with strengthened winds. This quiescent period is immediately followed by dramatic changes associated with the SSW which completely change the temperature and wind structure of the entire atmospheric column.

295 The developing SSW is seen in both the stratosphere and mesosphere, in both wind and temperature. $\overline{T_a}$ begins to rise in the stratosphere and fall in the mesosphere from the 26th of December, accelerating sharply from the 1st of January to reach a maximum (minimum) on the 4th of January with anomalies $|\overline{T_a}| > 25$ K from climatology. Coincident with this, \overline{u} at 60°N rapidly reverses over a few days at all heights above ~ 30 km, reaching zero at 10 hPa (32 km) on the 5th of January. This region of negative \overline{u} appears to extend through the stratosphere and mesosphere and continues above the top of the analysed region at ~ 90 km. Although MLS data are not validated for the top of our height range, a highly anomalous $u = -40 \text{ ms}^{-1}$ signal can be seen during this period at altitudes of ~ 80 km. In Supplementary Figure S2, we demonstrate that these negative zonal winds are consistent with observations above 80 km and above in data from made by the Esrange meteor radar ($68^\circ\text{N } 21^\circ\text{E}$, Supplementary Figure S3), suggesting that the MLS signal is likely real, where a highly anomalous $u = -40 \text{ ms}^{-1}$ signal relative to earlier parts of this winter is seen during this period.

305 After the zero-wind SSW criterion is reached, the stratosphere and mesosphere split into three distinct height-separated regimes, distinguished from each other by very different temporal patterns of $\overline{T_a}$:

- In the lower stratosphere, $\overline{T_a}$ slowly returns to climatology, dropping to < 10 K by day +20, < 5 K by day +30, and returning to climatology by late February (day +45). This corresponds to an extended period of low \overline{u} at these altitudes, with $|\overline{u}|$ only rarely exceeding 10 ms^{-1} . The upper limit of this region slowly descends with time.
- 310 – Above 60 km, temperature initially falls, reaching $|\overline{T_a}| < 5$ K by day +5 and -10 K by day +15. After this date we see a sharp rise, with $\overline{T_a} > 10$ K by day +22 and remaining consistently above this throughout February, again descending slowly with time. Variations in \overline{u} roughly correlate with $\overline{T_a}$ in this region.
- Around the stratopause, $\overline{T_a}$ initially falls rapidly, dropping > 45 K in three days in a mirror to the sharp pre-SSW rise. This decline slows at around day +4 and reverses at day +13, after which $\overline{T_a}$ begins to fall to reach < -15 K by day +22. This drop coincides with rising $\overline{T_a}$ in the mesosphere. From day +22 onwards, the temporal evolution of $\overline{T_a}$ closely mirrors the mesosphere for the rest of the studied period, with a descending boundary between the two regions related to a change in stratopause height discussed below. \overline{u} in this region is only weakly correlated with $\overline{T_a}$.
- 315

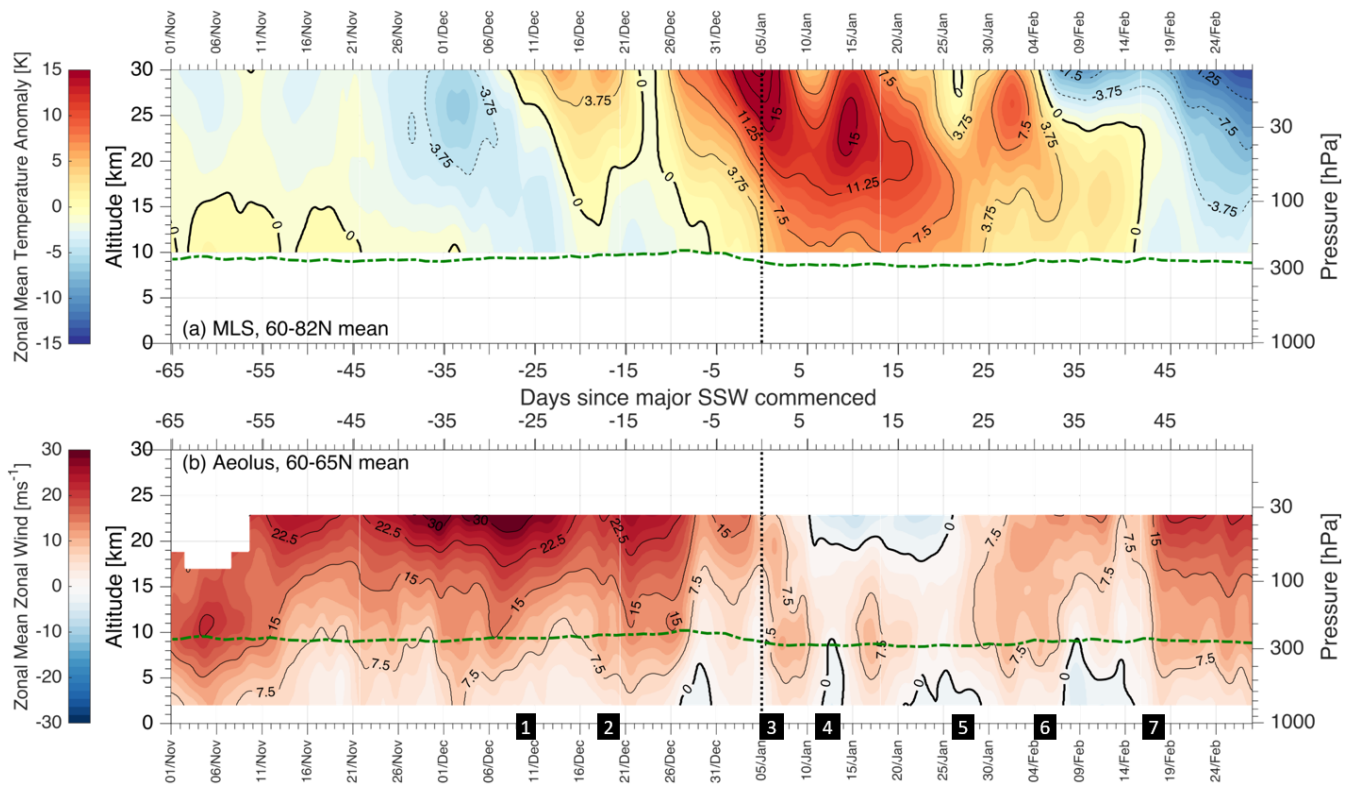


Figure 5. (a) MLS-derived 60°N–90°N mean temperature anomalies; (b) Aeolus-derived 55°N–65°N mean projected zonal winds for winter 2020/21, for altitudes 0–30 km. Mean tropopause height derived from ERA5 is shown as a dot-dashed green line. Vertical dotted line indicates the date at which 10 hPa winds reversed and the SSW became defined as major. Numbered boxes on the horizontal axis of (b) are used to guide discussion from Section 2.6 onwards.

Around day +30, the mean stratopause height rapidly jumps upwards by around 20 km; this is consistent with previous studies of upper-stratospheric SSW effects (e.g. Siskind et al., 2007; Manney et al., 2008; Wright, 2010; Wright et al., 2010; Manney et al., 2010; Wright et al., 2007; Manney et al., 2008; Wright, 2010; Wright et al., 2010; France and Harvey, 2013; Manney et al., 2015b), and is due to a new stratopause forming at high latitudes and altitudes rather than a sudden jump in the height of the original equator-connected stratopause (shown in zonal-mean MLS temperature in Supplementary Figure S1S3), likely due to the filtering out of orographic gravity waves by the lower-vortex near-zero winds. After this transition, the new stratopause continues to slowly descend for the rest of the studied period, forming a boundary between an unusually-cold stratosphere and an unusually-warm mesosphere. Tropopause height also exhibits a small amount of variability, falling by around 2 km immediately after the SSW begins and remaining below the pre-SSW height for the rest of the study period.

4.2 Winds and Temperatures in the UTLS and Troposphere

We next consider tropospheric and lower stratospheric \bar{u} as measured by Aeolus, Figure 5b. MLS \bar{T}_a is shown over the same height range in Figure 5a to help place our Aeolus results within the context of Figure 4. Note however that the vertical resolution of MLS in this height range is poor, with only 6 independent height bins in the range shown here. ~~Appendix ?? shows and discusses the same fields derived from ERA5 data, for comparison.~~

Strong positive \bar{u} is seen in the lower stratosphere from the beginning of November until the last week of December, with ~~slower weaker~~ but still positive \bar{u} in the troposphere ~~except in the lowest few kilometres of our data~~. Variations in \bar{u} occur approximately uniformly across the observed height range.

335 Starting around the 6th of December, \bar{u} falls at all heights for around ~~a week. This is approximately coincident with a similar short burst of ten days, with the later half of this period also exhibiting~~ increased \bar{T}_a , ~~suggesting that weakened winds are allowing some warming of the vortex; this~~. ~~This~~ \bar{u} and subsequent \bar{T}_a feature ~~propagates upwards from~~ ~~is visible first at~~ lower-tropospheric altitudes (Figure 5b) ~~rather than downwards from~~ ~~and then above rather than in~~ the middle atmosphere ~~and then below~~ (Figure 4b). Winds begin to increase in speed again around the 16th of December, this time with increased \bar{u} ~~propagating downwards from above~~ ~~visible first above then below~~, and stratospheric \bar{T}_a similarly returns to ~~normal~~ ~~median~~ ~~over the following few days~~.

From the 26th of December, a sharp drop in \bar{u} , ~~from a typical speed in the UTLS of~~ ~~is seen at all heights below 20 km: at the tropopause for example, the speed drops from~~ $\sim 15 \text{ ms}^{-1}$ to ~~around~~ $\sim 5 \text{ ms}^{-1}$, ~~is seen at all heights below 20 km~~. This marks the beginning of the SSW proper, as stratospheric \bar{T}_a also starts to rapidly increase at this date. As the SSW becomes major and the positive \bar{T}_a anomaly begins to propagate downwards into the lower stratosphere, we also see rapidly-dropping \bar{u} at the top of the Aeolus column, corresponding temporally with the same drop in MLS wind seen in Figure 4b.

\bar{u} at ~~25~~ ~~23~~ km altitude, the highest level observed by Aeolus, reverses (i.e. drops below zero) five days after it does so at 10 hPa, with the zero wind line descending ~~to reach a minimum altitude on the 15th of January, i.e.~~ ~~rapidly before stabilising at slightly below 20 km altitude until~~ day +10-20 from the SSW.

350 ~~From day +10 to day +20, the descending zero \bar{u} contour stalls at a minimum altitude of 19 km. Some variability around this level over the period of this minimum, with the absolute lowest altitude reached towards the end.~~ \bar{u} ~~below this remains suppressed, with the local maximum around the tropopause returning to pre-SSW levels around day +17. During this period, at altitudes below the zero-wind line remains much lower than earlier in the winter throughout this period;~~ \bar{T}_a meanwhile is large throughout the lower stratosphere, remaining above +7.5 K at most heights. This period of reduced winds corresponds to a period ~~where~~ the vortex is displaced by over 20° from the pole for an extended period, discussed in ~~Sections 7 and ??~~ ~~Section 7~~ below.

On days ~~Around day +21-+22~~ ~~23~~, wind speeds throughout the column begin to increase again, ~~rising by around 15 ms~~ ~~reaching as high as +10~~ ms^{-1} at 20 km on day +30-29 and higher than the preceding (i.e. peak-SSW) period at all heights ~~above 5 km altitude. This value represents a local maximum measured. This persists for about a week, after which \bar{u} again reduces to reach~~ a minimum at all heights on day +40. ~~This reduction is likely a downward-propagating response to a second drop below zero \bar{u}~~

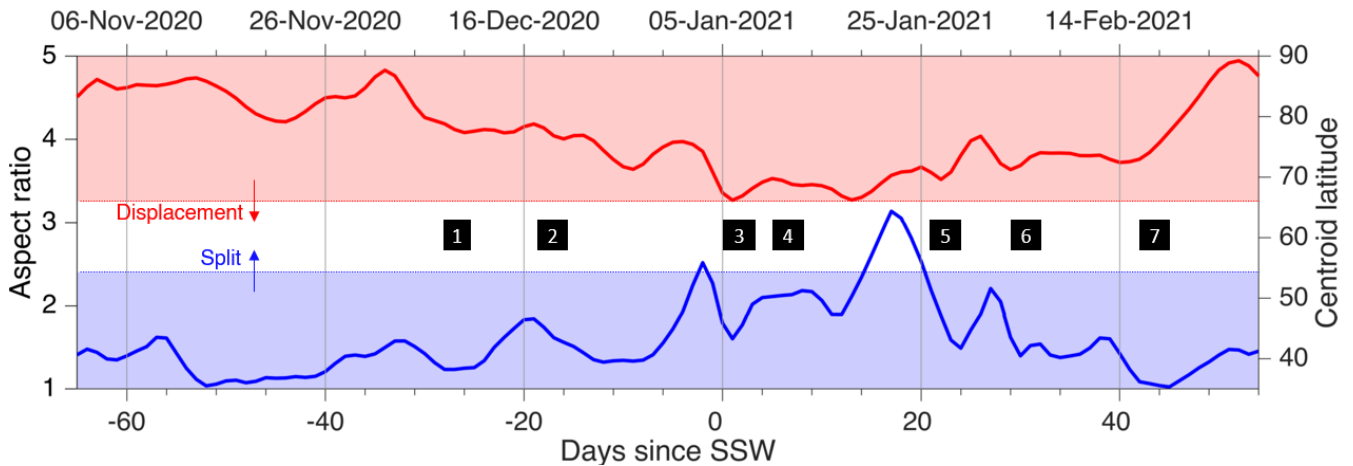


Figure 6. (red line) Centroid latitude and (blue line) aspect ratio of the polar vortex around the time of the January 2021 SSW, computed from ERA5 GPH at the 10 hPa level following the method of Seviour et al. (2013). Unshaded region indicates anomalous values indicative of a major vortex distortion, i.e. a split vortex for the blue line or a displaced vortex for the red line. Numbered boxes across the centre of the plot are used to guide discussion from Section 6 onwards.

~~at 10 hPa seen in reanalysis and operational analysis winds on the 4th of February (day +30; Figure 2a); note that, while a local minimum is also seen at this date in $\overline{MLS \bar{u}}$ (Figures 2a, 4b), observations do not quite reach zero. This minimum is near-zero in the lower stratosphere and below zero in the troposphere, but larger at the highest altitudes measured by Aeolus, and thus may represent a mixture of processes.~~

365 Finally, from day +40 onwards, wind speeds throughout the Aeolus column start to increase, and remain high for the rest of the study period. ~~This represents a steady transition back to a typical winter vortex, as seen in Section 3 using in reanalysis data~~ These values are unusually high for the year (Figure 3), which is typical of early major SSWs in the middle to upper stratosphere, and in the lower stratosphere in those that are early enough for the longer recovery times scales at those altitudes to have an effect before the spring final warming (e.g. Manney et al., 2008).

370 5 Split or Displacement?

SSWs are often categorised into splits, where the polar vortex divides into two or more sub-vortices, and displacements, where the vortex shifts off the pole but does not split (Charlton and Polvani, 2007; Mitchell et al., 2013). This distinction is important, as there is growing evidence from both model and observational studies that both the triggering processes and weather impacts of these two types of event can be quite dissimilar (e.g. Nakagawa and Yamazaki, 2006; Mitchell et al., 2013; Karpechko et al., 2017)

375 .

Figure 6 investigates the split/displacement nature of the early 2021 SSW, based on applying the vortex-moment diagnostics of Seviour et al. (2013) to daily-averaged ERA5 GPH at the 10 hPa level. The estimated centroid latitude of the polar vortex is

shown as a red solid line and the aspect ratio of the vortex as a blue solid line. By applying threshold criteria to these values, this method allows us to classify SSW events as a split or a displacement.

380 Seviour et al. (2013) empirically defined splits as events where the aspect ratio (blue line) remained ≥ 2.4 for seven days or more, and displacement events as those where the centroid latitude (red line) dropped equatorward of 66° for more than seven days. ~~Such classifications are typically made at~~ We have here restricted our discussion to the 10 hPa level ~~and we thus restrict our discussion here according; note that,~~ and note that the geometrical structure of the event may be different in the lower stratosphere, as has been found for previous SSWs Lawrence and Manney (2018). Even so, Figure 9, discussed below, shows
385 some evidence of vortex-splitting taking place at the ~~7082~~ hPa level.

The January 2021 SSW meets neither the split-event nor the displacement-event criteria of Seviour et al. (2013) at the 10 hPa level, but closely approaches both, making it a mixture of the two event types. This is reasonably common, with typically a third of SSWs being neither clear displacements nor splits (Baldwin et al., 2021).

The vortex centroid latitude never moves equatorward of 66° , but is equatorward of 69° for nine consecutive days from the
390 12th of January to the 20th of January. This period falls during the period of most negative zonal winds in the UTLS in our Aeolus data, and corresponds temporally to both strongly negative zonal winds at 60°N in MLS \bar{u} at 32 km (~ 10 hPa, Figure 4b) and in Aeolus \bar{u} 10 km below this (Figure 5b).

The vortex aspect ratio exceeds 2.4 twice, on the 3rd of January for one day and starting on the 20th of January for six days, but never meets the seven-consecutive-day element of the Seviour et al. (2013) criteria. Given we are using daily-averaged data
395 for this analysis, it is conceivable that there is a seven-day period offset from the diurnal cycle where the aspect ratio exceeds 2.4 which would allow us to tentatively class this SSW as a split warming; however, such a classification is marginal at best. Under the alternative criteria of Gerber et al. (2021), who first define events by zonal wind reversal and then subdivide into splits and displacements by the number of days in which the thresholds are exceeded within ± 10 days of onset, this event would be classified more directly as a split event.

400 6 Mesoscale Wave Forcing, in Reanalysis and Observations

~~The eddy heat flux $\overline{v'T'}$ and eddy momentum flux $\overline{u'v'}$, where the $'$ indicates deviations from the zonal mean and the overline an area-average, are widely used in atmospheric science to study the large-scale transport of heat and momentum by mesoscale waves and eddies. These parameters have significant implications for the stability of the polar vortex, and often prove useful in terms of forecasting how and when SSWs form. In particular, previous work has shown a clear relationship~~
405 ~~in reanalysis output whereby anomalously strong lower-stratospheric $\overline{v'T'}$ nearly always precedes weak vortex events such as SSWs (Polvani and Waugh, 2004)~~ The differing results of these two classifications highlights the inherent sensitivity of such threshold-based methods.

~~As Aeolus data provide systematic global-scale measurements of tropospheric and lower-stratospheric winds, they have the potential to help us estimate these fluxes entirely from observational data. To both assess this and to study the dynamical~~
410 ~~processes involved in this specific SSW, we here estimate $\overline{v'T'}$ and $\overline{u'v'}$ using Aeolus and MLS data and ERA5 output (Figure~~

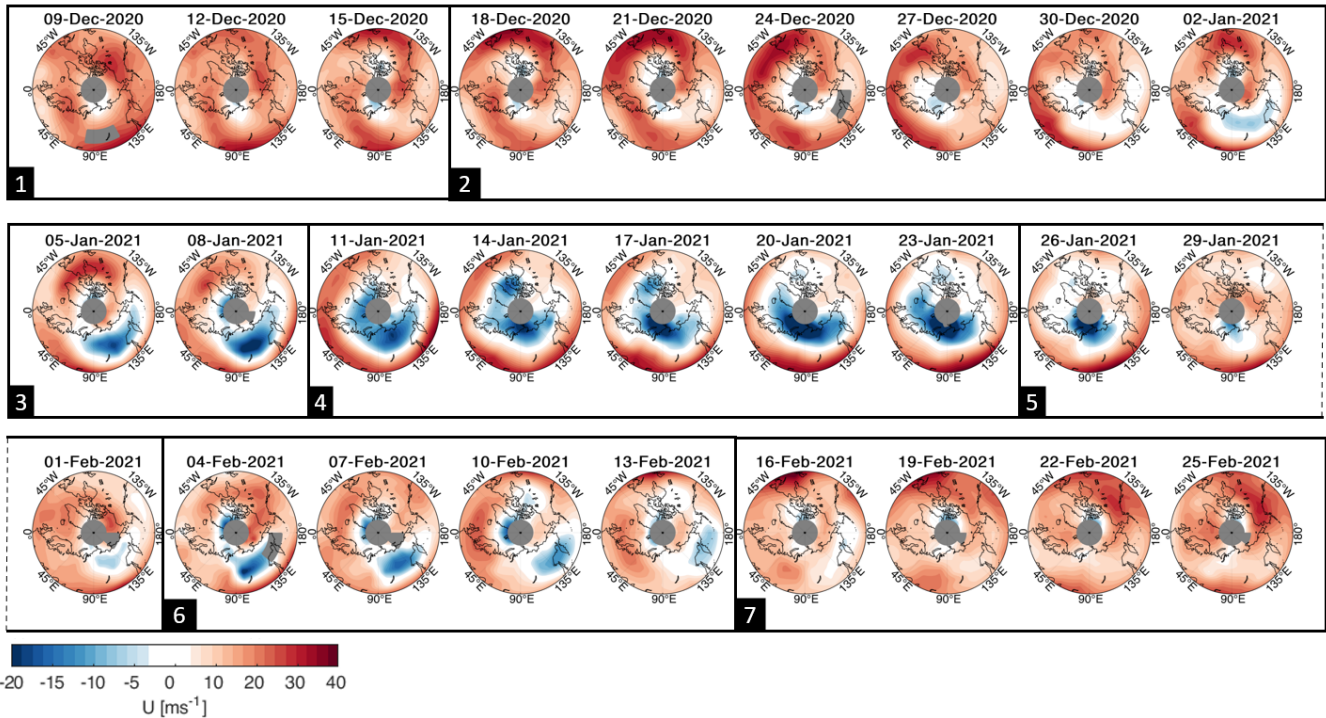


Figure 7. Eddy heat fluxes $\overline{v'T'}$ and eddy momentum fluxes $\overline{u'v'}$ estimated from MLS temperature data, Five-day-mean Acrolus wind data and ERA5 wind and temperature output, for three different combinations of these data sources: ‘ReA’ (all reanalysis, black), ‘Obs’ (all-observed, orange) and ‘Hyb’ (‘hybrid’, observed u and T with reanalysis v , blue). Data shown are averaged over the at 17 km altitude between 45°N–75°N latitude range, and shown at the (a,b) 50 hPa, (c,d) 100 hPa and (e,f) 150 hPa pressure levels 80°N. Observational series have been scaled by an empirically-chosen factor of $\times 10$. Pearson linear correlations r of Obs and Hyb with ReA are indicated at the top right of each panel. Colours show zonal wind speed; note asymmetric colour scale used to better highlight westward winds. Grey shading indicates the full range reanalysis-only daily estimates from all major SSWs between the 2004 and 2020 boreal summers. Numbered boxes indicate ‘phases’ of reanalysis-only daily estimates defined to help guide discussion.

??). These estimates are computed by first gridding the data onto a $2\text{ km} \times 30^\circ \times 10^\circ$ (height \times longitude \times latitude) grid, taking the difference of each point from the zonal mean, and then averaging the results over the $45^\circ\text{N}–75^\circ\text{N}$ region at each height to produce the time series shown. ERA5 output have been treated as individual points assigned to the centre of each model gridbox, in order to ensure full consistency in data treatment.

415 6 Vortex Structure at Sub-Zonal Scales

We compute three versions of $\overline{v'T'}$ and $\overline{u'v'}$. The first of these, labelled “ReA”, is computed entirely from reanalysis data. Given the large spatial scales involved in the analysis we assume for the purposes of this discussion that ReA represents a value close

to truth, and use it as a baseline for our other versions. Separately, we compute a fully-observational estimate, “Obs”, using
MLS and Aeolus u , v and T . Finally, in light of the significant uncertainties in v' identified in Appendix A, we show a further
420 estimate of $\overline{v'T'}$ and $\overline{u'v'}$, “Hyb”, which is a hybrid estimate computed using Aeolus u , MLS T , and ERA5 v to demonstrate
how a more robust Aeolus v' product could perform. We do not include an MLS-only time series due to our earlier decision to
only consider MLS geostrophic winds in the zonal mean (Section 2.2).

Figure ??a-f show (a,c,e) $\overline{v'T'}$ (b,d,f) $\overline{u'v'}$ time series at (a-b) 50 hPa (~ 21 km altitude) (c-d) 100 hPa (~ 16 km) and
425 (e-f) 150 hPa (~ 14 km). Observational series have been scaled by an empirically-chosen factor of 10 to compensate for the
methodological low bias in Aeolus v (Section 2). Pearson linear correlations between the hybrid and observed time series and
the reanalysis-only time series are shown at the top right of Figures ??a-f. All data have been boxcar-smoothed by three days
at the time series level (i.e. after computation of all variables) and the correlations have been computed from the smoothed
data; correlations of the unsmoothed daily data give proportionally similar results for the different time series but with smaller
numerical values, particularly for Obs which exhibits fractionally large day-to-day variability due to sampling pattern issues
430 but which is stable at the three-day-smoothed level.

To contextualise these data, we also show estimated $\overline{u'v'}$ and $\overline{v'T'}$ for the nine SSWs since August 2004. Following the
ERA-Interim derived estimates of Butler et al. (2017), we define these as having commencement dates of, consecutively,
2006-01-21, 2007-02-24, 2008-02-22, 2009-01-24, 2010-02-09, 2010-03-24, 2013-01-06, 2018-02-12 and 2019-01-02. These
events have each been individually processed using the same approach as our 2021 ReA estimates and their full range is
435 indicated by grey shading, with the black dotted line showing the distribution median.

At the start of October, $\overline{v'T'}$ is at the low end of the nine-SSW climatology at all levels. At 50 hPa, there is a brief burst
of negative $\overline{v'T'}$ in Obs 80 day before the SSW, but not in ReA or Hyb. This deviation grows and shrinks smoothly over
several days, lasts long enough that it is unlikely to be due to sampling bias, and represents a sign change in v relative to the
surrounding period which reprojecting HLOS wind into the v -direction should be robust against (Appendix A). Thus, this may
440 represent a real difference between ERA5 and true v . A brief period of negative $\overline{v'T'}$ is also seen at the 100 hPa and 150 hPa
levels around day -50, which is consistent across the three times series but with lower amplitude in Hyb and ReA. $\overline{u'v'}$ in
October shows large oscillations about zero, but the amplitude of these oscillations is broadly consistent with our nine-SSW
climatology at all heights, and of roughly the same magnitude between levels (note the different vertical scales).

As we move into November, we begin to see $\overline{v'T'}$ oscillations with periods of approximately one week in all three time
445 series at 150 hPa level, overlying a positive overall trend. The 100 hPa level shows similar behaviour with approximately the
same magnitude of oscillation, while at 50 hPa we see some variability but with a smaller amplitude and larger positive trend
relative to the oscillation amplitude. $\overline{u'v'}$ during November continues to oscillate significantly and with a larger amplitude than
in October, with an underlying shift to a higher and then lower medium-term (\sim fortnightly) mean at all three levels.

Things begin to change in early December. In $\overline{v'T'}$, we see a positive overall trend from around day -40 until immediately
450 before the beginning of the SSW in January. This trend, albeit interrupted by a sharp dip of around one week in mid-December,
is visible and clear at all three levels and is consistent with our expectation of strong $\overline{v'T'}$ before an SSW. With the exception
of the dip, values are almost exactly at the median for our nine-SSW climatology (black dotted line), with the same positive

trend. While the dip represents an outlier from this trend, it is only slightly outside the full range of the climatology in the negative direction for a few days in Obs and not at all in ReA and Hyb.

455 $\overline{u'v'}$ during this period also trends lower, and is also largely within climatology except for a brief period at lower levels which coincides with the dip in $\overline{v'T'}$; this suggests that the dip is being driven by changes in v' rather than u' or T' . This dip in both series coincides with a brief shift in the 10 hPa vortex towards a more elliptical vortex (Figure 6) centred at 80°N between north Greenland and Russia (Figure 9, discussed below), and the negative v' anomaly is consistent with disrupted flows during this period seen over Eurasia and the Pacific in maps of Aeolus wind at 17 km altitude (Figure 7, also discussed below).

460 At the beginning of January, all-height $\overline{v'T'}$ and 50 hPa $\overline{u'v'}$ both drop significantly, reaching their smallest values across the entire period to date. This drop in $\overline{u'v'}$ is at the lower limit of climatology for $\overline{u'v'}$ and significantly outside it for $\overline{v'T'}$, representing unusual mesoscale behaviour for the start of an SSW—in particular, the median of our climatology suggests that $\overline{v'T'}$ at this point would normally be at a maximum relative to several months on either side of the beginning of an SSW. This is anomalous, and may perhaps suggest that the initial increase in \overline{T} could have been driven by the mean flow rather than eddies.
465 After ~10 days the eddies do seem to drive a strong warming though.

A few days after the SSW formally commences, we see sharp rises in $\overline{v'T'}$ and 50 hPa $\overline{u'v'}$, back to slightly above pre-SSW values, moving from significantly below the climatological range to slightly above it, and from around the 10th of January (day +5) until early February these values remain anomalously high, reaching a time-series maximum a few days after the vortex returns to its normal aspect ratio range at 10 hPa following a six-day split (Figure 6). From this point, both variables begin
470 oscillating strongly, and over the next two weeks they drop from a time-series maximum well above climatology to a time-series minimum well below, then back to a maximum above. This degree of variability is highly anomalous, with the oscillations in this single year larger than the entire data range over this period seen around the last nine SSWs. The oscillations roughly follow shifts in the vortex aspect ratio and centroid location at the 10 hPa level above (Figure 6), and correspond to varying zonal-mean upper-tropospheric winds (Figure 5) related to a short attempt by the vortex to return to its normal morphology
475 which ultimately fails (Section ??). $\overline{u'v'}$ at the 100 hPa and 150 hPa levels differ from the other four time series for the January period, remaining well inside climatology, but share the precipitous drop and subsequent rise seen in early February.

Finally, in late February we see a return to typical post-SSW values. This is consistent with the largely normal wind speed seen during this period in e.g. Figures 4 and 5. As in October, $\overline{v'T'}$ is once again at the lower end of climatology but still within it, and $\overline{u'v'}$ is close to the distribution median.

480 Based on these results, we draw three conclusions for future calculations of $\overline{v'T'}$ and $\overline{u'v'}$ using Aeolus-type wind data and equivalent supporting temperature data such as that from MLS, and two conclusions about mesoscale eddy forcing during the 2021 SSW.

1. *Aeolus* Current one-dimensional observations with Aeolus and MLS can clearly identify the large relative changes in $\overline{v'T'}$ and $\overline{u'v'}$ associated with SSWs, albeit with a very large ($\sim \times 10$) but consistent error in magnitude. Relative to
485 reanalysis, the observations diverge from background at the same time, show the same oscillations both large and small, and correlate well (at three-day smoothing, >0.8 in most cases and ~ 0.7 at worst) given the potentially large pointwise errors in our inferred u and v .

2. *Aeolus* Hybrid products using reanalysis-derived v show exceptional correlation with pure reanalysis estimates, highlighting the high quality of *Aeolus* u and MLS T .
- 490 3. *Aeolus* It is necessary to significantly spatially average *Aeolus* v data to perform such an analysis. Calculations of $\overline{v'T'}$ and $\overline{u'v'}$ on narrower spaced grids in latitude (not shown) exhibited much larger deviations from the reanalysis and hybrid estimates, consistent with the large uncertainty on v .
4. *Eddy forcing* Eddy forcing was normal for momentum flux but appears to be anomalous for heat flux, where we appear to see a time minimum during the SSW onset. While we do not calculate a detailed heat budget here, if correct this may suggest that the increase in stratospheric temperatures near SSW onset are a result of changes in the mean flow rather than eddy driven.
- 495 5. *Eddy forcing* The January 2021 SSW was also unusual in the degree of variability seen after the initial outbreak of negative 10 hPa winds, with very large oscillations seen relative to climatology in $\overline{v'T'}$ and $\overline{u'v'}$. These oscillations approximately correspond temporally to an initial recovery of the vortex and subsequent return to SSW conditions for a few days.
- 500

7 Vortex Structure at Sub-Zonal Scales

While the zonal mean is often a useful tool for broadly characterising the atmospheric state, it can disguise important local variations in atmospheric structure. To better understand the dynamical changes to UTLS and tropospheric wind patterns induced by the 2020/21 SSW, in this Section we examine geographic variations in (a) *Aeolus* winds in the UTLS and troposphere and (b) ERA5 GPH at the 10 hPa and 70 hPa levels.

505

6.1 The 3D Polar Vortex in *Aeolus* Winds

Figures 7 and 8 illustrate the geographic structure of *Aeolus* derived polar winds during the 2020/21 SSW in 2D. Figure 7, 8 and 9 illustrate the temporal development of *Aeolus* u and 3D respectively. MLS GPH over the course of the SSW.

Figure 7 shows *Aeolus* u at 17 km altitude. This altitude level is selected as it is typically the highest altitude level where *Aeolus* data coverage continues equatorward of 60°N (Figure 1), allowing the maps to extend further south than this latitude for broader context. The maps show consecutive five-day means, stepping three days between each panel. Three-day and one-day means were separately assessed: one-day means do not provide full geographic coverage, while three-day means gave broadly the same results but with more noise. For clarity of discussion, we define seven approximate ‘phases’; these phases are typified by the selected dates in Figure 8, each of which corresponds to multiple panels in Figure 7 identified by a labelled box for each phase of the SSW’s lifecycle, which are indicated by numbered boxes on the Figure. These phases (for time series, indicated at an approximate midpoint rather than either their commencement or the typical days shown in Figure 8) are also shown and labelled on Figures 5 b, 6, 9 and 10 to provide context throughout the study.

510

515

Five-day-mean Aeolus wind at 17 km altitude between 45°N and 80°N. Colours show zonal wind speed; note asymmetric colour scale used to better highlight westward winds. Overlaid arrows show wind vectors, computed from u and v ; v has been scaled by an empirically-chosen factor of $\times 10$. To highlight patterns, arrows are consistently sized within each panel but not between panels. Numbered boxes indicate ‘phases’ of the SSW, defined to help guide discussion.

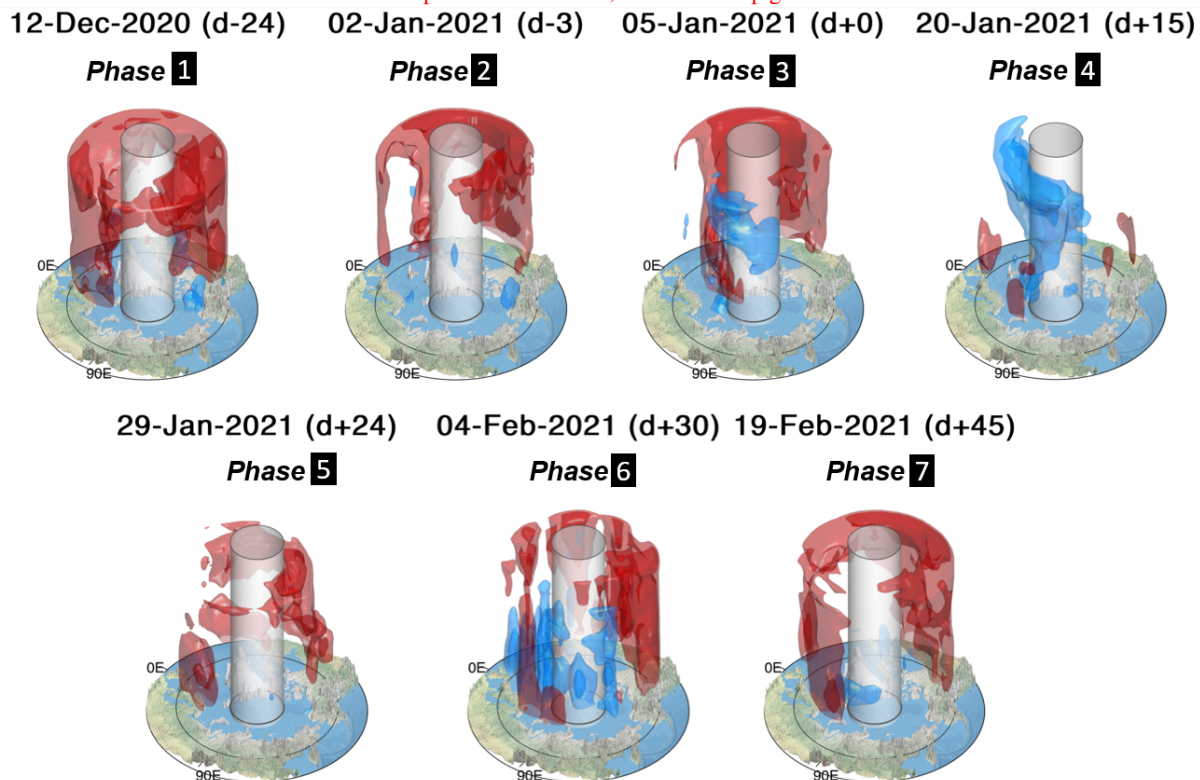


Figure 8. Three-day-mean Aeolus u between 60°N (indicated by a line at surface level) and 80°N (indicated by the outer surface of the central semi-transparent grey cylinder) for selected dates during winter 2020/21. Values in brackets after each date indicate day numbers relative to the 5th of January 2021. Outer red (blue) surfaces enclose regions with wind speeds $>15 \text{ ms}^{-1}$ in the eastward (westward) direction; interior red (blue) surfaces enclose regions with wind speeds $>25 \text{ ms}^{-1}$. Terrain is shown at true relative height, using mean values on a $10 \text{ km} \times 10 \text{ km}$ regular spatial grid centred at the pole. Isosurfaces have been closed at the limits of the plotted volume for visual clarity, but are very likely to extend beyond it in the real atmosphere.

Three-day-mean Aeolus u between 60°N (indicated by a line at surface level) and 80°N (indicated by the outer surface of the central semi-transparent grey cylinder) for selected dates during winter 2020/21. Values in brackets after each date indicate day numbers relative to the 5th of January 2021. Red (blue) surfaces enclose regions with wind speeds $>10\text{ ms}^{-1}$ in the eastward (westward) direction. Data are plotted from 5 km to 22 km altitude on a 0.75 km vertical grid. Terrain is shown at true relative height, using mean values on a $10\text{ km}\times 10\text{ km}$ regular spatial grid centred at the pole. Isosurfaces have been closed at the limits of the plotted volume for visual clarity, but are very likely to extend beyond it in the real atmosphere.

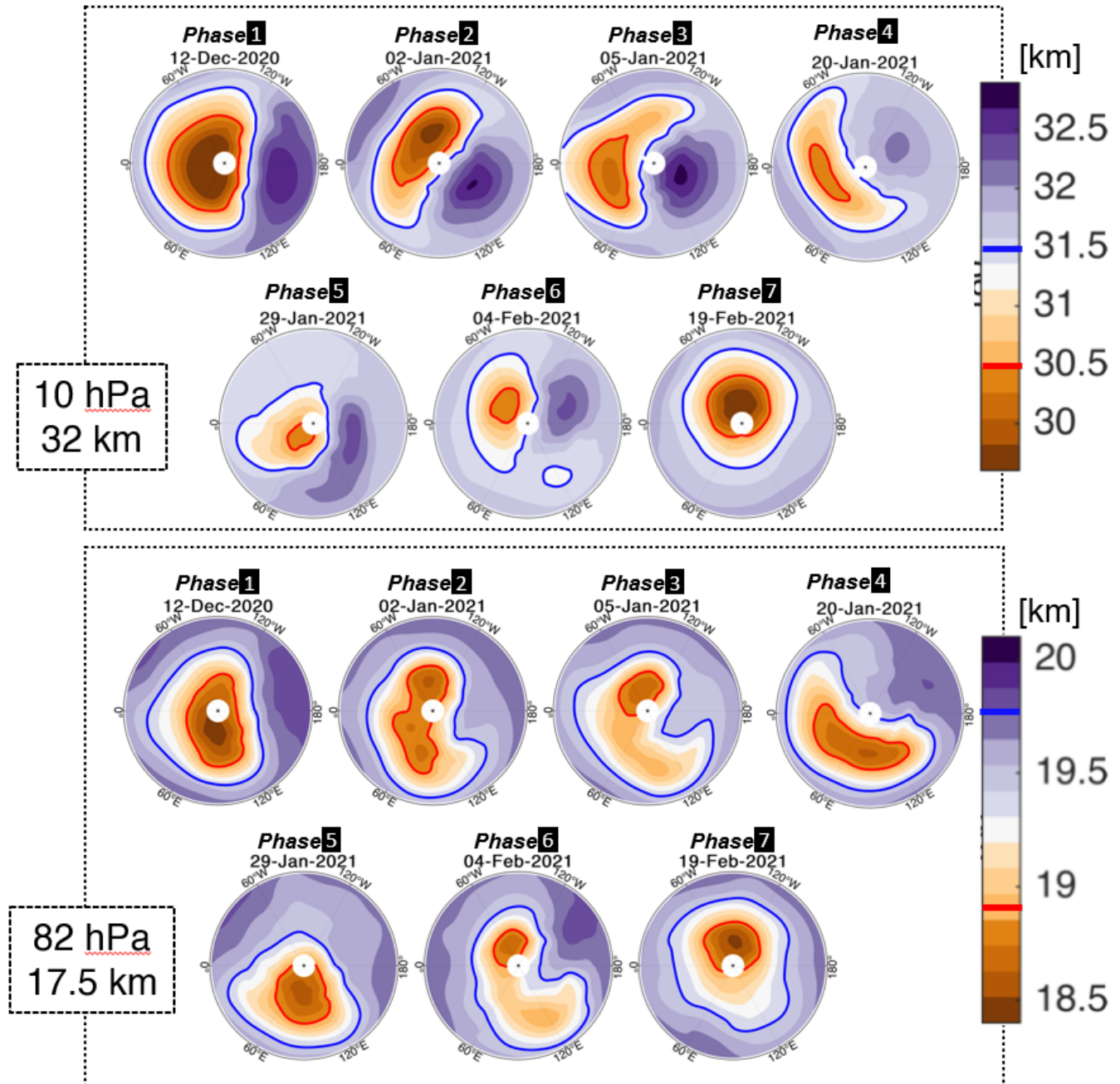


Figure 9. Maps of MLS (top) 10 hPa (bottom) 82 hPa GPH in km for selected day. Selected contours have been highlighted in blue and red, with their locations indicated on the colour bars.

Figure 7 shows Aeolus-derived u and v for consecutive five-day periods between December 2020 and February 2021 at 17 km altitude². This altitude is the highest where coverage consistently extends equatorward of 60°, allowing us to contextualise the vortex changes in the horizontal domain. Colours show zonal wind speed; vector arrows show relative wind speeds and absolute directions after v has been scaled by a factor of 10. Three-day-means were separately assessed, and gave broadly the same results for u , but with much more noise in arrow direction due to large uncertainties in v ; one-day means do not provide full geographic coverage⁶ for context, with the numbered boxes on these figures indicating the start dates of the phases identified in Figure 7.

Figure 8 shows three-day-mean Aeolus-derived shows five-day-mean Aeolus u for our seven selected dates seven dates selected as representative of their Phase. Equivalent plots for all dates shown in Figure 7, providing are included as Supplementary Figure S4 to provide a more complete three-dimensional overview of the SSW evolution, are included as Supplementary Figure S2 but not discussed further here. The data are plotted inside a volume covering the region poleward of 60°N from heights of 5–22 km, and are shown as 3D concentric isosurfaces set at $u = +10 \text{ms}^{-1}$ (red) and -10ms^{-1} (outer red), $+25 \text{ms}^{-1}$ (inner red), -15ms^{-1} (outer blue) and -25ms^{-1} (inner blue). Surface topography maps are shown at the base of each volume, and are to true vertical scale with the winds; these maps extend beyond the polar regions for context, with the 60°N southern data limit indicated by a grey circle at surface level. A semi-transparent grey cylinder fills the region poleward of the northern data limit at 80°N.

Figure 9 shows maps of (upper half) 10 hPa and (lower half) 82 hPa altitude MLS GPH for the same dates. The 10 hPa level is chosen for consistency with the general literature on SSWs and Figure 6. The 82 hPa level is chosen as the closest standard MLS pressure level to the 17 km altitude level shown in Figure 7 (82 hPa \sim 17.5 km). Empirically-selected contours intended to highlight the shape of the GPH minima are shown in red and blue.

Throughout this Section we refer to both the 17 km data in Figure 7 and the 82 hPa data in Figure 9 as being at 82 hPa, in order to make clear that we are treating these data as being at the same vertical level, to reduce confusion between kilometres as both a unit of GPH and altitude, and for clarity of prose.

The SSW evolves over our seven phases-Phases as follows.

1. [*Pre-SSW Beginnings*]: In phase-Phase 1, the polar vortex is strong and mostly circular. Maps has started to drift off the pole and deform, with an aspect ratio ~ 1.3 and centroid latitude of 78°N at 10 hPa (Figures 6 and 9). At 82 hPa, the vortex-centre GPH minimum is also deformed, with a minimum value at 77°N, 79°E and with noticeable elongations into Europe, Canada and (especially) Central Asia. Zonal winds are strong and positive around this minimum at the 82 hPa level (Figure 7) show uninterrupted and strongly positive u ; vector winds flow in a near-zonal circle around the pole. The except for a local minimum over the Sea of Okhotsk late in the Phase, $u > +10 + 15 \text{ms}^{-1}$ surface almost completely occupies the plotted volume except at the lowest altitudes at all heights within the 60°-80°N volume except for this region and the region of minimum GPH itself (Figure 8). Local u in the vortex-edge winds reaches values $u > +2530 \text{ms}^{-1}$ over Alaska. While u during this period is atypically strong relative to our climatology (Section 3), the

²At time of submission, a daily-animated version of this figure is available from the European Space Agency website,

observed morphology is ~~typical for winter Aeolus data~~. The vortex in GPH at this time has already slipped slightly off the pole (Figure 6 and Section ??), but otherwise this period is broadly consistent with our theoretical understanding of the undisturbed winter atmosphere ~~similar to Aeolus data~~ from earlier in the winter (not shown).

555 2. [*Vortex Breakdown*]: In late December and early January, the ~~UTLS vortex begins to break down~~. At 17 ~~vortex centroid~~ latitude moves steadily equatorward ~~and~~ with the aspect ratio remaining consistently above 1.4 at both the 10 km hPa and 82 hPa levels. As January begins, the vortex elongates along an axis aligned from the Caspian Sea to Hudson Bay, briefly exceeding an aspect ratio of 2.4 at the 10 hPa level (Figure 6), and multiple independent local minima appear in 82 hPa GPH over northern Canada and over the Arctic Ocean north of Russia and (separately) Scandinavia (Figure 9). At 82 hPa, we see patches of first white and then blue appearing, ~~corresponding to~~ in Figure 7, representing localised regions of ~~rapidly-decelerating near-zero and reversing~~ u . The broad GPH minimum's morphology can also be inferred in these Aeolus winds from ~~positive- u flows over mainland Canada and negative- u flows~~ over Russia. Zonal mean \bar{u} remains positive (Figure 5) ~~is still positive~~, but a significant fraction of the polar volume now has $u < +10$ 15 ms^{-1} and small regions ~~have reached~~ ~~reach~~ $u < -10$ 15 ms^{-1} . ~~There is some suggestion of a developing split into two subvortices, one centred over northern Canada and the other over the Arctic Ocean north of Russia, inferred from positive- u flows over mainland Canada, negative- u flows over Russia, and the direction of the vector winds near the 80°N data limit. Such an interpretation is consistent with our reanalysis-derived vortex metrics (Section 5) and with the morphology of the 70 hPa GPH field (Section ??), both discussed further below~~ at low altitudes (Figure 8).

570 3. [*Onset*]: ~~A major SSW is declared as~~ The major SSW begins as zonal mean winds at 10 hPa, 60°N reach zero; this occurs around 10 km above the top of our ~~measurement volume~~ Aeolus measurement volume but can be seen in MLS geostrophic and ECMWF operational and reanalysis winds (Figure 2). By this time, ~~a large fraction of polar UTLS u has already reversed~~. A helical structure begins to develop in wind (Figure 8) ~~has already reversed in a large large fraction of the polar UTLS (Figure 7), spreading outwards from a locus over Siberia which corresponds to a local (but not global) minimum in 82 hPa GPH (Figure 9). Over the next two weeks (i.e. throughout Phases 3 and 4) the vortex remains at its southernmost point and is highly elongated, with a negative GPH anomaly stretching from western Russia and Scandinavia over the North Atlantic and (in the early part of the period) Canada. This period represents the maximum of lower-stratospheric \bar{T} and the minimum of 60°N \bar{u} (Figures 4 and 5), i.e. the peak of the SSW. A volume of positive $u > 15 \text{ ms}^{-1}$ at high altitudes over North America and low altitudes over northwestern Russia underlying wraps around a volume of negative $u < -15 \text{ ms}^{-1}$ at high altitudes over Scandinavia which grows to extend to all altitudes above northeastern Russia. At, and at the centre of the region of negative u , zonal wind speeds have reached values as low as~~ $u < -15 \text{ ms}^{-1}$ at 17 ~~82 km hPa~~.

580 4. [*Peak SSW*]: ~~Here~~ During this Phase, the SSW is in full swing in ~~has major effects on winds throughout~~ the lower stratosphere. ~~The earlier attempt at splitting the vortex appears to have failed, and instead near-uniform~~ Near-uniform negative u is seen in all areas poleward of 60° at 17 ~~82 km altitude hPa (Figure 7), with the exception of a small region over Alaska. This phase~~ Phase corresponds to the negative \bar{u} patch seen in Figure 5b at altitudes above 19 km, and

585 to the large positive temperature anomaly seen at these heights in Figure 5a. The ~~he~~ heal-spiral wind structure seen in phase Phase 3 remains, but with ~~a large reduction in the volume~~ the almost complete elimination of regions occupied by ~~$u > +10$~~ 15 ms^{-1} and a large increase in the volume with ~~$u < -10$~~ 15 ms^{-1} . ~~The region of $u > +10$~~ During this Phase, the ~~winds closely following the form of the 82 ms^{-1} above North America has completely disappeared, and the region of~~ $u < -10$ ~~hPa GPH minimum, with eastward flows south of the region enclosed by the 18.8 ms^{-1} above Russia and Europe~~ has grown significantly. ~~km GPH contour (red line) and westward flows north of the region. This period corresponds to the latter part of the displacement-like period in Figure 6.~~

- 590
5. *[Initial Recovery]*: The polar vortex begins to recover in late January. ~~We~~ In the latter part of this Phase, we see positive u at all locations at ~~1782 km~~ hPa except for a small region over the northern Pacific. ~~(Figure 7)~~ This corresponds to the local maximum in \bar{u} seen in Figure 5, and represents an initial attempt by the vortex to ~~spin back up.~~
 - 595 6. *Second Onset*: In Figure 2, we see a secondary minimum in MLS and reanalysis \bar{u} at 32 km at the start of this phase. Over the following days, \bar{u} reduces at all heights (Figure 5b), and a negative u region in Figure 7 over Russia develops again, together with a jumble of positive and negative u volumes over Europe and the seas north of Great Britain. A second patch of negative wind also briefly develops over Canada towards the end of this phase in the 17 km maps.
 7. *Final Recovery*: Finally, the vortex returns to normal. By the end of this phase, the UTLS atmospheric flow is again strong and circular around the pole, and values of $u > 10$ ~~ms^{-1}~~ fill most of the volume. This state is very typical for polar stratosphere at this time of year (Figure 3), thus representing a return to near-normality, albeit with significant anomaly temperatures at altitudes above our wind data (Figure 4a).
- 600

6.1 Vortex Temporal Evolution

605 Maps of ERA5 (top) 10 hPa (bottom) 70 hPa GPH in m for selected days at 00:00. Selected contours have been highlighted in blue and red, with their locations indicated on the colour bars. Aeolus wind vectors at 17 km and poleward of 40° have been overlaid on the lower panel, and the continents removed to aid visual interpretation. Wind vectors have been scaled in the v direction by a factor of $\times 10$.

610 Figure 9 show maps of (upper half) 10 hPa and (lower half) 70 hPa ERA5 GPH. The data have been plotted at the seven dates previously selected in Figure 8, and an additional date one month before phase 1 has been included to show the pre-SSW form of the vortex. Empirically-selected contours intended to highlight the shape of the vortex and to help guide our discussion below are shown in red and blue. return to a more symmetrical form. The 10 hPa level is chosen for consistency with the general literature on SSWs and Figure 6. The 70 hPa level is chosen as the closest model-output pressure level to the 17 km altitude level shown in Figure 7 (70 hPa ~ 18.5 km; recall that our Aeolus data is binned onto a 2 km grid).

615 17 km altitude Aeolus wind vectors have been overlaid on the lower panels; as previously, the v component of Aeolus wind has been empirically scaled by a factor of $\times 10$. Wind vectors equatorward of 40°N have been omitted; this is

620 because wind speeds in the midlatitude jet are significantly faster than in many regions nearer the pole, and visually dominate the Figure if included. These wind vectors follow the contours of the vortex edge in GPH exceptionally closely at all timepoints shown given the assumptions implicit in our reprojection into u and v , again demonstrating the high fidelity of Aeolus wind products.

The temporal progression of the vortex can be followed clearly through these maps and the summary lines shown in Figure 6. We divide this discussion into three distinct narrative sections, as follow.

6.0.1 Pre-SSW, Phase 1

625 In mid-November, the 10 hPa vortex is roughly circular and centred very close to the pole. It begins to drift south over the next few weeks, briefly bouncing back towards the pole at the very beginning of December (Figure 6). By the 12th of December (phase 1 map) the vortex centre has clearly moved, but is still centred relatively near the pole at 78°N , approximately on the prime meridian. This first six weeks of data correspond to the period of largely typical stratospheric weather seen at the left hand side of Figure 4.

630 At the 70 hPa level the vortex is less regular in form, consistent with expected atmospheric dynamics at this height. It is somewhat irregular in shape in November, and has started to elongate along the 120°E axis by the 12th of December. Aeolus wind vectors follow the edge of the GPH-derived vortex contours closely, including a tight detour towards the pole slightly east of the prime meridian in November.

6.0.1 Vortex Breakdown, Onset and Peak SSW, Phases 2–4

635 The equatorward drift of the 10 hPa vortex core begins to accelerate at the end of December, again interrupted by a brief movement poleward (Figure 6). As January begins, the vortex elongates along an axis aligned from the Caspian Sea to Hudson Bay, briefly exceeding an aspect ratio of 2.4 (Figure 6). A few days after this, the zonal mean wind speed at 60°N reaches zero and the SSW becomes major. Over the next two weeks the vortex remains at its southernmost point and is highly elongated, with a negative GPH anomaly stretching from western Russia and Scandinavia over the North Atlantic and (in the early part of the period) Canada. This period represents the maximum of lower-stratospheric \bar{T} and the minimum of $60^{\circ}\text{N} \bar{u}$ (Figures 4 and 5), i.e. the peak of the SSW.

640 At 70 hPa the vortex splits at around the 17.4 g.km contour during phase 2, deepening to the 17.3 g.km contour (red line) in phase 3, and exhibits separate but joined minima over Canada and central Russia, with the saddle between the minima lying over the Arctic Ocean east of Greenland. By phase 4 this bipolar structure has dissolved, leaving a clear single minimum spanning mainland Russia. This minimum is centred 45° east of the 10 hPa GPH minimum over Scandinavia; consistent with the helical wind structure seen in the lower half of this altitude range in Figure 8.

645 Wind vectors in these snapshots continue to closely mirror the vortex edge. In phases 2 and 3, wind data suggests that either two separate circulations or a single circulation in close to the form of a figure-8 have formed flowing anticlockwise

around the two minima; unfortunately due to lack of data coverage at the very highest latitudes we do not observe the region where these circulations would meet.

650 During phase 4, we again see winds closely following the form of the 70 hPa vortex core, with eastward flows south of the region enclosed by the 17.3 g.km contour (red line) and westward flows north of the region. Winds speeds (i.e. arrow lengths) inside the contour are significantly lower than those to the south, and slightly smaller than those to the north. Winds on the other side of the pole are both relatively (Figure 9) and absolutely (Figure 7) low in this period, contributing to the near-zero GPH minimum at 60°N during this period (Figure 5). This period corresponds to the latter
655 part of the displacement-like period in Figure 6.

6.0.1 Initial Recovery, Second Onset, and Final Recovery, Phases 5–7

In phase 5, the vortex core at 10 hPa shifts this date has shifted eastwards and slightly northwards, becoming more circular and centred over the Arctic ocean poleward of north-central Russia with an extension into Eastern Europe. At the 7082 Pa level, it hPa level, the GPH minimum is centred slightly southeast of the 10 hPa centre, and also forms a
660 single less-elliptical mass more-circular area covering most of Russia. Winds are strong and zonal along the southern edge of the vortex core, and in general flow anticlockwise around the region of minimum GPH. Wind speeds are large on the south side of the vortex and small on the other side of the pole. 82 hPa GPH minimum.

As we move into phase 6, we again see a brief attempt by the vortex to split at both levels; at the 10

8. [Second Onset]: In Figure 2, we see a secondary minimum in MLS and reanalysis \bar{u} at 32 hPa level this occurs at the
665 29.8km at the start of this Phase. Over the following days, \bar{u} reduces at all heights (Figure 5b), and a negative u region at 82 g.km contour (blue line), while at hPa over Russia develops again (Figure 7), together with a jumble of positive and negative u volumes over Europe and the 70 seas north of Great Britain. A second patch of negative wind also briefly develops over Canada towards the end of this phase in the 82 hPa level we again see a saddle forming over Greenland which splits the data at the 17.3 g.km contour (red line). This snapshot has the poorest correspondence between GPH and the wind vectors of the eight snapshots: while we again see some evidence of either two separate or one figure-8
670 circulations at the 70 hPa level around the minima in GPH, the winds in the Canadian minimum are strong and northwards and those at the northern edge of the Russian minimum are more disrupted and less clearly flowing around the minimum than in our other snapshots. This may be an artefact of time-averaging the Aeolus data; phase 6 varies rapidly in form (Figures 7–8) and while we have shown a single timepoint for model GPH, we have used a five-day averaging for our
675 wind vectors which may not be respond quickly enough to the evolution of the geophysical situation to match the GPH contours. Such a problem would also affect phase 5, our shortest phase, but as the situation is less rapidly-varying there we do not see a mismatch hPa maps.

Finally, in Phase 7, we see a return to normal winter conditions

9. [Final Recovery]: Finally, the vortex begins to returns to a more typical, if still slightly disturbed, state. At both the 10 hPa and 70~~82~~ hPa levels, the vortex is centred slightly south of, but close to, the pole, with minimum GPH along the 80°W meridian but poleward of 85°. ~~Winds at the 70°N, 82 hPa level winds~~ are maximal close to ~~the longitude of, but slight west of,~~ the vortex minimum ~~and on the mirror-, with a secondary maximum on the opposite~~ side of the ~~vortex~~ GPH minimum, and follow contours of GPH likely associated with a weak high-mode planetary wave (light purple). By the end of this phase values of $u > 15+ \text{ms}^{-1}$ fill most of the polar volume. This atmospheric state is broadly typical for the zonal mean polar stratosphere at this time of year (Figure 3), albeit with significant anomaly temperatures at altitudes above our wind data (Figure 4a).

7 Surface Coupling and Surface Impacts

SSWs often have significant effects on surface weather. These effects typically take place through indirect coupling processes over the weeks following the SSW, including via modulation of the jet stream, the Northern Annular Mode, and other processes ~~which~~ imprint upon GPH (e.g. Baldwin and Dunkerton, 2001; Kidston et al., 2015; **Ming, 2015**).

To investigate such coupling, Figure 10a shows normalised area-weighted polar-cap-mean GPH anomalies (hereafter Z') averaged from 65–90°N derived from ERA5 data relative to a 1979–2020 climatology. ~~Note that this climatological period differs from our previous analyses, which use the post-2004 MLS period only~~ ERA5 GPH is used here rather than MLS GPH as above to provide seamless coverage down to the surface and a longer climatological record.

695 We first describe the temporal evolution of Z' in the UTLS and above.

- Absolute stratospheric Z' does not exceed 1 until the last two days of December. Z' is negative at the beginning of December, turns positive in mid-December, then becomes negative again until near the end of the month. The positive Z' period corresponds to the beginning of the vortex breakdown (Figures 5, 7, 9), ~~and happens at approximately the same time as minima are seen in both $\overline{u'v'}$ and $\overline{v'T'}$ at all heights (Figure ??), with the minimum at the start of the Z' peak in $\overline{u'v'}$ and the end in $\overline{v'T'}$.~~
- From the 26th of December, Z' increases at all heights. This happens first in the UTLS, where it coincides with falling Aeolus \bar{u} (Figure 5). A few days later, Z' also begins to increase above 30 km, at the same time as MLS \bar{u} rapidly reverses (Figure 4). These separate regions of high Z' both spread vertically into the lower stratosphere with time, converging at ~ 20 km altitude around the start of the SSW as the vortex centroid reaches its most southerly point and becomes highly elongated (Figures 6 and 9).
- As the SSW evolves, stratospheric Z' remains high for an extended period, with lower-stratospheric $Z' > 1.75$ for twenty days and > 0 for over forty days after the SSW commences. In the upper stratosphere, we see $Z' > 0$ for most of this period, with a small local maximum at $\sim +25$ days corresponding ~~again to strong local minima in $\overline{u'v'}$ and $\overline{v'T'}$ at all heights (Figure ??) and to~~ to a brief period of increased \bar{u} in Figure 5.

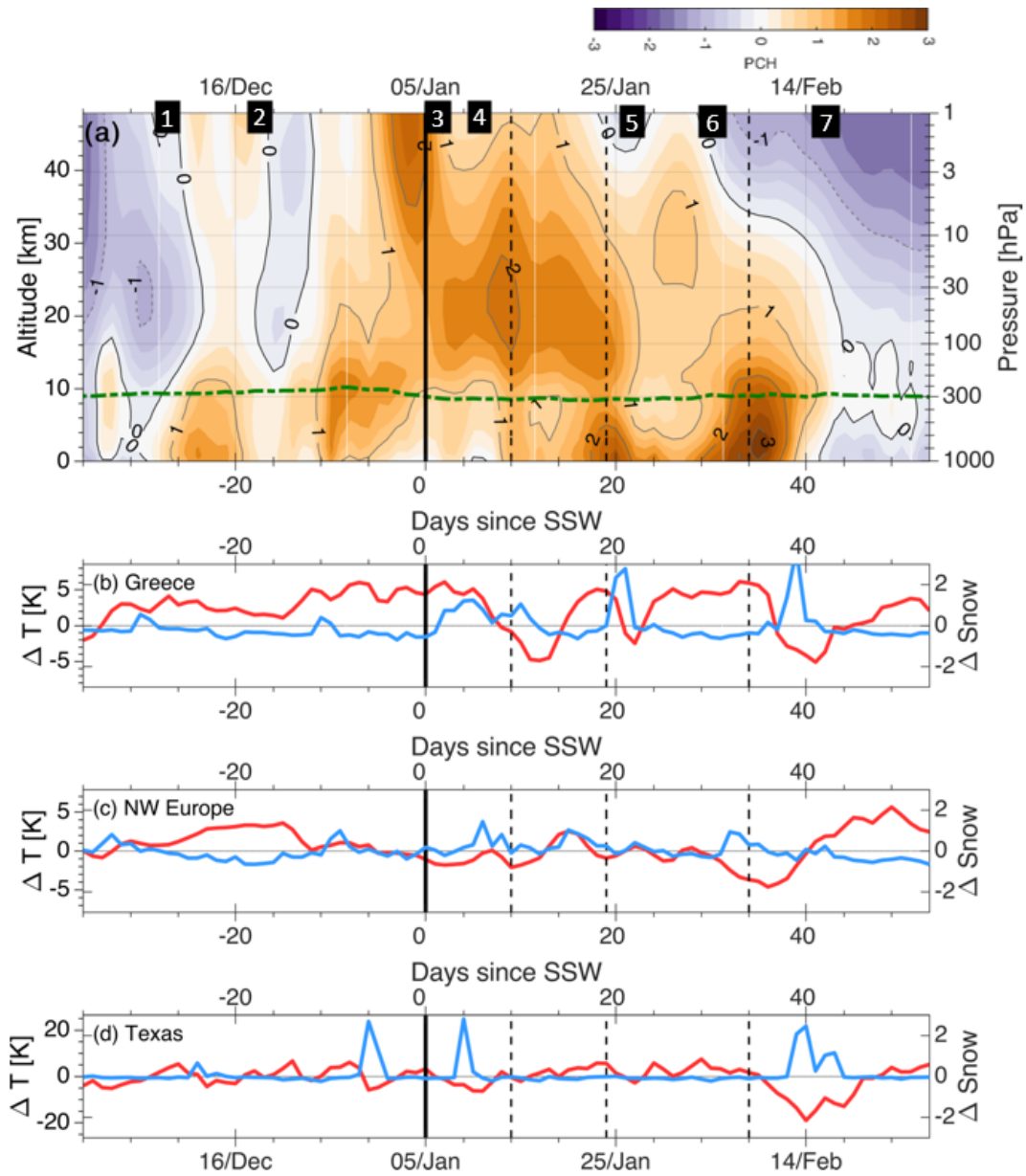


Figure 10. (a) Polar cap height anomalies (Z') around the January 2021 SSW relative to a 1979–2020 climatology, derived from ERA5 GPH. Green dash-dotted line indicates tropopause height. (b-d) time series of (red, left axis) 2 m temperature anomaly and (blue) fractional snow cover extent for three selected geographic regions. For all panels, the thick solid vertical line indicated the 10 hPa date of the SSW commencing, and the thin dashed lines corresponding to local post-SSW minima of Z at zero altitude. Numbered boxes refer to SSW phases discussed above.

710 – From the beginning of February, Z' begins to fall, crossing 0 at the beginning of February at the top of the shown height range and continuing to reach -1.75 by the end of the month. This decline begins at the highest altitudes before propagating downwards, and coincides with zonal wind speeds throughout the column returning to climatology.

We next investigate how the SSW may have coupled to and impacted upon surface weather, using Z' as a proxy metric of stratosphere-troposphere-surface coupling. Z' is a good proxy for the Northern Annular Mode (NAM) Index, which indicates the strength of the polar vortex through the stratosphere, and surface impacts are approximately proportional to the anomalous strength of the polar vortex in the lower stratosphere (Baldwin and Dunkerton, 2001; Baldwin et al., 2021). In the troposphere, the NAM index is a good indicator of the jetstream response at this level.

To quantify surface weather effects, Figure 11 shows map consecutive five-day-mean 2 m temperature anomaly-anomalies (hereafter 2mT') maps and 500 hPa level geopotential height (hereafter '500GPH') anomalies at the hemispheric scale from the beginning of the SSW to the end of February. Supporting our discussion, we also (Figures 10b-d) show fractional-snow-cover extent-snow cover anomalies and 2mT' averaged over Greece (specifically, 20-30°E, 35-45°N), Northwestern Europe (10°W-20°E, 45-65°N), and Texas (105-95°W, 45-65-25-35°N). 2mT' has and the snowfall anomalies have been derived from ERA5 output; snow cover extent has been produced by interpolating weekly values from Robinson et al. (2014) to a daily scale. 2mT' in Figures 10 and 11 is are again computed relative to a 1979–2020 climatology.

725 We structure our discussion in terms of Figure 11, referring to Figures 10b-d to highlight some selected specific events with a strong possibility of stratospheric linkages.

From the 7th of January, we see negative 2mT' over Western Europe, associated with extreme snowfall in Madrid and the surrounding area (not shown) the heaviest snowfall in Spain for over 50 years. Based on both the early date of this event relative to the SSW lifecycle and on the lack of any obvious Z' feature linking the stratospheric vortex breakdown to the surface (Figure 10a), we believe that this event was not caused by the SSW. The cooler average temperatures in Europe prior to and around the commencement of the SSW are however consistent with the work of Kolstad et al. (2010) and King et al. (2019). There are notable regions of positive 2mT' over Siberia and the Arctic Ocean, and North America, which weaken and strengthen respectively by 12th January and are congruent with positive 500GPH anomalies.

By the 17th of January, 2mT' surface structures characteristic of SSW surface impacts have begun to appear (e.g. Butler et al., 2017), with a cold anomaly in Siberia and a warm anomaly over Baffin Bay, associated with positive and negative 500GPH anomalies respectively. This follows the development of a positive Z' link from the lower stratosphere to the surface (first dotted line from left, Figure 10). Over the days following this Z' link, we also see reduced 2mT' and anomalously heavy snowfall over Greece (Figure 10b), together with a local maximum in snow cover extent and minimum in 2mT' over NW Europe (Figure 10c). A negative NAO-like pattern is evident over the Atlantic from 22nd January, although the centres of action shift during the subsequent weeks. This is indicative of a southward shift in the jet stream, which is associated with cold air outbreaks over Europe.

740 From the 27th of January, negative 2mT' begins to appear over the mainland United States, and positive 2mT' in the Middle East, simultaneously with a low-latitude-low-altitude maximum of $Z' > 2$ (Figure 10a), both of which are components of the typical SSW surface signal in 2mT' (Butler et al., 2017). An unusual feature here is the development of positive 2mT' over the

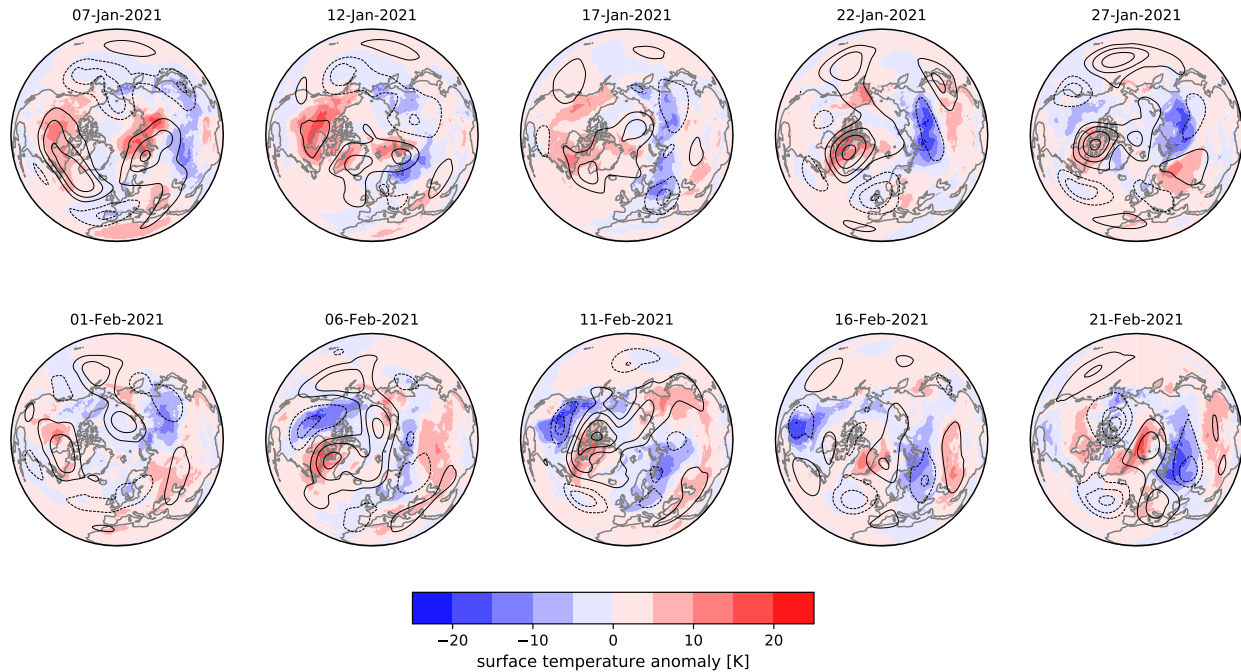


Figure 11. Consecutive five-day-mean maps of ERA5 2 m temperature (shading) and 500GPH (contours) anomalies for the period following the SSW. Values are shown as anomalies from a 1979-2020 climatology for the given dates. 500GPH contours are at 100 m intervals, negative values are dashed, and the zero contour is omitted.

745 Urals, which persists into early February and is associated with high pressure over the Urals advecting warm air from the south. This feature may have acted to inhibit westward extension of Siberian cold anomalies, and prevented northeastern Europe from developing a strong cold anomaly before this date.

From the 1st of February, cold 2mT' moves southward over North America, starting over Alaska and western Canada, then intensifying over the mainland United States and reaching Texas by 11th Feb. This US cold air outbreak was the coldest
 750 February weather in this region since 1989, and can be clearly seen in Figure 10d as a very large negative 2mT' (~-20 K relative to climatology) with high-snow-coverage, which commences a number of days of high snowfall anomalies which commence synchronously with a strong positive $Z' > 3$ and in turn suggests a strong possibility of a role for stratosphere-troposphere coupling. The cold outbreak was intensified by increased high pressure over the Aleutian region which acted to block the jet stream, causing associated with a southward loop of the jet downstream of the block and advecting cold air southwards (Figure
 755 11). The increased Aleutian high here may have been in part due to pre-existing La Niña conditions in the tropical Pacific

during this winter; furthermore, increased blocking, seen in the 500GPH anomalies for 1st -11th February (Figure 11) over the Canadian Archipelago, may have acted to push cold further south than usual.

Northwestern Europe experiences its most intense cold spell from the 1st to the 11th of February, also synchronously with this large Z' anomaly. A local-minimum temperature was reached at Braemar on the 11th of February, which **at 250 K** was the lowest UK temperature since 1995. ~~This cold air shifts~~ These cold anomalies shift eastwards by the 16th of February, ~~delaying the explaining the delay in the~~ development of cold snowy weather in Greece relative to NW Europe, and leading to Athens experiencing 20-25cm of snow on the 15th and 16th of February.

Although data of this type cannot show a direct causal link, our data ~~therefore~~ strongly suggest that the early January SSW may have acted as either a trigger or an intensifier for several extreme winter weather events affecting densely-populated regions of the Northern Hemisphere over the next two months. **Even if the SSW did play an important role in these extreme events, our analysis is also not able to explain why different regions may have been impacted at different times during the SSW evolution; such an investigation is left to future studies.**

8 Summary and Conclusions

~~In the Introduction, we outlined two key objectives for this study, which were to (1) characterise SSW-induced dynamical changes for this event using novel observational data and (2) to assess the suitability of Aeolus data for studying future extreme weather events of this type. Accordingly, we divide our discussions and conclusions between these two headings. we have used Aeolus Rayleigh-clear wind data, MLS temperature and GPH data, and ERA5 temperature, wind, GPH and snowfall output to study the evolution of the early-2021 northern hemisphere sudden stratospheric warming event.~~

8.1 Objective 1: Dynamical Changes and Impacts

~~Unlike many others~~ Under the empirical criteria of Seviour et al. (2013) which we we apply here, this SSW was a **mixed event** not easily classifiable as having either a split or a displacement vortex. ~~Considering for example the criteria of Seviour et al. (2013) , the vortex was displaced for mixture of split and displacement types, with the vortex displaced~~ long enough but not far enough south to be a displacement event, and with an aspect ratio elliptical enough but for too brief a period to be a split event.

~~At a bulk climatological level, the SSW was fairly typical, with zonal mean~~ Zonal mean temperature and wind anomalies were broadly within the climatological range of other 21st-century SSW events (Section 3): while date-maximum temperatures and ~~winds in the normal range for such an event (Section 2.4). However, closer study identifies atypical features, including a second zero-crossing of 60°-10hPa wind nearly a month after commencement associated with a recovering and then re-collapsing vortex (Section 6), and highly anomalous mesoscale eddy forcing during and after the event (Section ??)~~

~~Aeolus wind data strongly correlate spatially with GPH estimates from ERA5, supporting their accuracy. The GPH estimates, in turn, show evidence of downward coupling supporting the hypothesis that several major extreme weather events during January and February 2021, including cold and snow cover extent extrema in Greece, Northwestern Europe and, especially,~~

Texas were likely related to some degree to the SSW at the beginning of the year. This demonstrates the large and significant impact of SSWs on surface climate, and highlights the importance of improving our stratospheric forecasting capabilities.

8.1 Objective 2: Assessments of Aeolus Data

790 ~~Aeolus data-minimum zonal winds were seen during the event relative to a 2004-2020 climatology, these values were broadly consistent with the anomalies seen during other 21st century SSWs with different commencement dates.~~

~~This study represents the first use of Aeolus data to study an SSW, and one of the first scientific uses of this unique dataset, the first systematic measurements of global-scale winds in the free troposphere and lower stratosphere. We demonstrate that Aeolus Rayleigh data are suitable for scientific use in studying dynamically-extreme events such as SSWs. Even using inherently-limited estimates of u and v reprojected from 1D data and (in the case of v) only approximately scaled for magnitude, Aeolus wind agrees well with both MLS and observed winds agree well with those inferred from MLS GPH and simulated by ERA5 (Section 2.4), supports direct estimation of mesoscale fluxes consistent with reanalysis (Section ??), produces and the high spatial resolution of the product allows us to produce maps showing detailed and internally-consistent 2D and 3D wind structure (Section ??, and shows 6). These maps also show excellent agreement at a physical level with the evolution of the vortex in ERA5 MLS GPH (Section ??6).~~

795
800

~~Aeolus data contain The Aeolus data also clearly exhibit relatively fine vertical structures. A key example of this are the helical wind features, including a pole-wrapping wind feature seen in Figure 8 during phases 3, 4 and 6, which represent structures the peak of the SSW, which is only a few kilometres in vertical extent at any given height and remains visible in the data even after applying heavy vertical (2 km), horizontal ($5^\circ \times 20^\circ$) and temporal (three-day five-day) averaging to ensure full coverage. Although we do not do so here, exploitation of the Aeolus Rayleigh data at its true spatiotemporal resolution and of the even finer-resolution Mie data could provide additional useful information on possible filamentary wind structures related to the vortex breakdown of before and during the SSW.~~

805

~~Aeolus consistently measures much higher zonal-mean wind maxima in the bursts of positive zonal wind seen in the UTLS before the SSW (Figure 5, Appendix ??). This suggests that Finally, study of ERA5 has difficulty reproducing short bursts of high winds relative to observations.~~

810

~~Aeolus winds may contain features not present in ERA5 output, although these differences could well be due to Aeolus measurement errors (including due to day-to-day changes in spatial sampling) or errors induced by our reprojection, and more detailed study will be required to confirm if they are real. Two main examples of this are seen in this study, (a) a period of internally-consistent sign difference from reanalysis $\overline{v'^T}$ (Figure ??a) and (b) a several-day differences in timing the timing of when zonal-mean \bar{u} reached zero at the top of the Aeolus column (Figure 2); the minimum \bar{u} reached in observations is also deeper and longer-lasting. In the later case, MLS geostrophic u provides supplementary evidence of this being an error in the reanalysis GPH and snowfall output in the context of the SSW (Section 7) suggests that this SSW coupled downwards to the surface, and support the hypothesis that several major extreme-weather events during January and February 2021, including cold and snow cover extent extrema in Greece, Northwestern Europe and, especially, Texas were likely related to some degree~~

815

820 [to the SSW at the beginning of the year. This demonstrates the large and significant impact of SSWs on surface climate, and highlights the importance of improving our stratospheric forecasting capabilities.](#)

Code and data availability. Aeolus data can be obtained from the ESA Aeolus web portal, <https://aeolus.services/>. MLS data can be obtained from the NASA DISC, <https://disc.gsfc.nasa.gov/>. ERA5 data can be obtained from the Copernicus Climate Data Store <https://cds.climate.copernicus.eu/>. The code used to produce the analyses and figures has been archived at doi:10.5281/zenodo.4638273.

825 *Author contributions.* CJW developed the concept of the study, carried out most of the data analyses presented, wrote the initial draft of the manuscript, and produced all figures except Figure 11. RJH carried out the vortex-moment analyses for Figure 6, the surface-coupling analysis for Figure 10, and produced and analysed the data for Figure 11. TPB acquired and preprocessed the Aeolus data used, and carried out vital work underpinning the data analysis pipeline. NPH implemented and wrote the text describing the wind calculation method described in Appendix A), based on the idea of and with the advice of IK. All authors contributed to understanding and interpreting the data and to
830 finalising the manuscript text.

Competing interests. The authors have no competing interests.

Acknowledgements. CJW, DMM, NPH and RJH are funded by NERC grant NE/S00985X/1. CJW is also funded by Royal Society University Research Fellowship UF160545, and DMM by NERC Independent Research Fellowship NE/N014057/1. TPB is funded by EPSRC grant EP/R513155/1 and by Royal Society grant RGF/EA/180217.

835 **Appendix A: Projecting HLOS Wind into the Zonal Deriving estimated zonal and Meridional Directions meridional winds from Aeolus HLOS wind measurements**

~~Aeolus measures the~~ The horizontal line-of-sight (HLOS) wind measured by Aeolus is a projection of the horizontal zonal and meridional wind vectors u and v in the HLOS direction. In this study, we project the measured HLOS wind into zonal and meridional components to obtain u_{HLOS} and v_{HLOS} u and v into a single along-line-of-sight direction.

840 ~~Figure ?? illustrates the geometry of this process, where θ is the azimuth of the HLOS direction measured clockwise from north. The Aeolus~~ The measured HLOS wind u_{HLOS} is the sum of projections from both the zonal and meridional winds as the two components

$$\text{HLOS wind} \equiv u_{\text{HLOS}} = - (u \sin \theta + v \cos \theta), \quad (\text{A1})$$

~~Our projected winds u_{HLOS} where θ is defined as the reflex angle measured from north to the direction along the line-of-sight of the ALADIN instrument. Because the lidar points at a 90° angle to the direction of travel, this results in a different projection during ascending ('asc') and v_{HLOS} are then given by descending ('desc') nodes of the orbit, specifically~~

$$u_{\text{HLOS}} = u \sin^2 \theta + v \sin \theta \cos \theta$$

$$v_{\text{HLOS}} = u \sin \theta \cos \theta + v \cos^2 \theta$$

850 ~~$u_{\text{HLOS, asc}} = u \sin(\theta) + v \cos(\theta)$~~ (A2)

~~$u_{\text{HLOS, desc}} = u \sin(-\theta) + v \cos(-\theta)$~~ (A3)

~~We can see from the above that u_{HLOS} and v_{HLOS} are not independent, and it is possible for u_{HLOS} to be contaminated by projections of the meridional wind v and vice versa. However, since tropospheric u is typically larger than v , and the angle θ is greater than 70 degrees equatorward of 70°N , we can estimate that this effect is likely to be small for u_{HLOS} . If we~~

855 ~~define a latitude-longitude-height-time box, we can estimate the true (i.e. unprojected) average horizontal zonal and meridional wind vectors \bar{u} and \bar{v} for this box by averaging all HLOS wind measurements that fall within the box for both ascending and descending orbits. This uses the different information content of the two scanning directions to cancel out directional uncertainties in measurement. For the average meridional wind vector \bar{v} , we compute this as~~ Schematic diagram showing the Aeolus horizontal line of sight (HLOS) viewing geometry, where θ is the angle between the HLOS direction and north. When

860 ~~Aeolus makes wind measurements, the zonal and meridional wind vectors u and v are projected into the HLOS direction. This~~

measured HLOS wind then projected into u_{HLOS} and v_{HLOS} shown throughout the study.

$$\begin{aligned}\bar{v} &= (u_{\text{HLOS, asc}} + u_{\text{HLOS, desc}}) / 2 \cos \theta \\ &= (u \sin \theta + v \cos \theta + u \sin(-\theta) + v \cos(-\theta)) / 2 \cos \theta \\ &= (2v \cos \theta) / 2 \cos \theta\end{aligned}$$

865 $\equiv v$ (A4)

To further constrain any errors due to this ambiguity, we have assessed the differences between and for zonal wind \bar{u} as

$$\begin{aligned}\bar{u} &= (u_{\text{HLOS, asc}} - u_{\text{HLOS, desc}}) / 2 \sin \theta \\ &= (u \sin \theta + v \cos \theta - u \sin(-\theta) - v \cos(-\theta)) / 2 \sin \theta \\ &= (2u \sin \theta) / 2 \sin \theta\end{aligned}$$

870 $\equiv u$ (A5)

We use this method to estimate u and u_{HLOS} and between v and v_{HLOS} for ERA5 reanalysis winds. To do this, we first sample u and v from ERA5 at the times and locations of all Aeolus measurements in January 2020, then project these into the satellite observation frame of reference to estimate the HLOS wind, then project this back into cardinal directions to estimate u_{HLOS} and v_{HLOS} .

875 Aeolus-sampled ERA5 estimates of u , v , u_{HLOS} and v_{HLOS} (a,e,i,m) show u , (b,f,j,n) u_{HLOS} , (c,g,k,o) v_{HLOS} and (d,h,l,p) v at (a-d) 20 km, (e-h) 15 km, (i-l) 10 km and (m-p) 5 km.

Figure ?? shows these sampled fields at four height levels. Sampled u_{HLOS} (second column from left) corresponds well in terms of both morphology and magnitude with the input u field (first column). Sampled v_{HLOS} shows similar morphology to the input v field, but with a much smaller magnitude: v_{HLOS} (third column) is typically a factor $\sim 10\times$ smaller than the input v fields (fourth column) at any given point.

880 Estimated error $u - u_{\text{HLOS}}$ due to projection from HLOS to direction-resolved wind, computed using the Aeolus January 2020 sampling pattern and ERA5 reanalysis winds. (a,d,e,h,i,l,m,p) probability distribution of pointwise error as a function of latitude for (a,e,i,m) zonal (d,h,l,p) meridional winds. (b,c,f,g,j,k,n,o) maps of mean error for (b,f,j,n) zonal (c,g,k,o) meridional winds.

885 Figures ??(a,e,i,m) and (d,h,l,p) show the same data as probability distributions of pointwise differences ERA5 $u - u_{\text{HLOS}}$ and $v - v_{\text{HLOS}}$ respectively, as a function of latitude at four height levels. In each panel, five grey lines are shown, indicating (from top to bottom) the for all Aeolus measurements presented in this study, with our boxes defined to each cover a region of 2.5th, 18th, 50th (median), 82nd and 97.5th percentiles of the pointwise distribution. These percentiles are chosen as they represent the non-parametric equivalents of the first and standard deviations of a normally-distributed dataset.

890 For $u - u_{\text{HLOS}}$, differences are small near the Equator at all altitudes, increasing with latitude. This is consistent with Aeolus' orbital geometry, which will have a meridional LOS at the polar turnaround latitudes and a near-zonal LOS at the

Equator. Accordingly, the width of the distribution increases dramatically at the poles, with the 2.5-97.5% range reaching a width of $\pm 20 \times 22.5^\circ$ in latitude and longitude respectively and 2 ms^{-1} at high altitudes. Importantly, however, the majority of the measurements remains tightly distributed around the zero-difference line (black-dashed), with the median diverging only by low single-digit values at all heights, and the 18-82% range reaching widths of at most 10 km in height - this box size is chosen to give full geographic coverage at a daily level. To improve vertical resolution at a small cost of point-to-point independence, we step the boxes in height at intervals of 1 ms^{-1} . There is a positive skew to the distribution, indicating a tendency to overestimate the true zonal wind using this technique in this region; 2019/20 was a record-strong year for the polar vortex from late January onwards (Lawrence et al., 2020), and thus the equivalent errors for our 2020/21 study may be more evenly split by sign than in this test case.

Reprojected meridional winds perform much worse than zonal at most latitudes, with an 18-82% range approaching $> 20 \text{ ms}^{-1}$ at most latitudes. This is consistent with the very large magnitude differences seen in Figure ??.

Figures ??(b,c,f,g,j,k,n,o) map the mean differences in the (b,f,j,n) zonal and (c,g,k,o) meridional directions, again at four height levels. In the zonal direction, these mean differences are typically $< 3 \text{ ms}^{-1}$ at most locations and heights, except at the 20 km altitude level where they routinely exceed 5 ms^{-1} . A systematic positive skew is seen in most cases, consistent with the probability distribution.

Meridional geographic mean differences are much larger and evenly split between positive and negative differences, with values approaching and sometimes exceeding 20 ms^{-1} at all heights. The meridional pattern seen corresponds extremely closely in both spatial pattern and amplitude to an underlying pattern in meridional wind seen in ERA5 output during this period (Figure ??, rightmost column); this is because removing the very small-magnitude v_{HLOS} magnitudes from the original v fields makes only a marginal difference to the final results.

Based on this analysis, we conclude that the use of projected zonal winds is in general safe for our analysis provided not too much scientific weight is placed on individual point-values; that is to say that the data are largely reliable when averaged across several individual points. Projected meridional winds, however, are much less robust, and in particular cannot be safely used for individual-point analysis. They do however have a broadly correct morphology at large length scales, and therefore can be of scientific use provided they are averaged over large areas and account is taken that wind magnitude will be very heavily suppressed. Although we do not investigate it directly here, v_{HLOS} estimates may be of more scientific use in the tropics, where the spread range narrows markedly; this is consistent with the observational geometry of the satellite, as the line-of-sight vector will be directed in km. To compute zonal mean winds, we apply the same method, but using a near-meridional direction near the Equator. 360° box width in longitude.

Appendix B: Differences between ERA5 and Observations in the Zonal Mean

ERA5-derived (a) 60°N – 90°N mean temperature anomalies; (b) 55°N – 65°N mean zonal winds for winter 2020/21, for altitudes 0–30 km. Mean tropopause height is shown as a dot-dashed green line. Vertical dotted line indicates the date at which 10 hPa winds reversed and the SSW became defined as major.

925 Difference between Figures ?? and 5. Data have been smoothed three days in time to compensate for satellite sampling patterns.

Figure ?? shows zonal-mean ERA5 (a) temperature and (b) winds, in the same graphical form as MLS and Aeolus data in Figure 5. Figure ?? shows the same data as a difference from the equivalent observations. The data used in Figure ?? have been smoothed by three times before differencing, as daily differences exhibit significant For most figures shown in this study, we
930 uses boxes with a width of one day in time, except in Section 6 where we use sliding five-day fits as described there. These temporally wider boxes have reduced point-to-point noise and hence allow relatively detailed spatial mapping, but at a cost of day-to-day noise which we assume to be due to satellite spatial sampling independence.

At a broad level, the data are highly similar in the zonal mean, with deviations not exceeding 3A fundamental assumption of this method is that any given ascending scan samples broadly the same wind field over a given region as the subsequent
935 descending scan (or vice-versa). This assumption can be broken down into three distinct error sources: (1) the heterogeneity of the background wind over the spatiotemporal extent of the box; (2) the spatial separation between ascending and descending scans within that box, which varies with latitude and can be as much as $2000 \text{ K} / 4\text{ms}^{-1}$ except for a small number of poorly-sampled bins at the very top of the Aeolus column. In general, ERA5 reproduces MLS temperature well with differences falling approximately evenly to either side of zero. Differences are also spread around zero for wind, but with a clear bias
940 towards higher wind speeds in Aeolus.

ERA5 \bar{T} and \bar{U} are significantly smoother than the observational data, consistent with their origin in an assimilative model. The period of only small temperature anomalies and timing of the repeated speeding up and slowing down of the vortex edge winds in November and early December are well-reproduced by the reanalysis, but the maxima of wind speed in this bursts are significantly underestimated by the reanalysis, with these maxima representing the largest differences outside the top binning
945 level km in the tropics; and (3) the separation in time between ascending and descending scans, which can be as much as 12 hours in local time. This means that longitudinal gradients in wind speed at scales of hundreds of kilometres, or significant changes in wind speed over timescales of less than 12 hours, will introduce errors in the winds computed using this method, as the above assumptions can become invalid. At high latitudes, such as those presented here, the spatiotemporal separation between measurements is relatively low, and thus these three sources of error are all minimised, but will be larger at lower
950 latitudes. In particular, we do not expect systematic differences between measurements during daytime and nighttime since the effects of atmospheric tides are weak at the altitudes considered here, significantly ameliorating (3).

The extreme temperature variations of the SSW are well reproduced by ERA5, despite the physical complexity of the event, with differences remaining below 3 K. After the SSW, a long-lasting high-bias is seen in ERA5 relative to MLS covering most of the lower stratosphere (i.e. a negative difference MLS-ERA5), lasting until winds begin to accelerate again at the end
955 of January. The reduction and reversal of zonal winds at the top of the Aeolus column is much shallower in both depth and magnitude in ERA5, and the region of enhanced wind around the tropopause shortly after the SSW is split into two distinct regions. The speeding up and slowing down of the lower-stratospheric vortex after the SSW is well-reproduced in ERA5, as is the final restoration in late February, again with a notable low-bias in ERA5's ability to produce short-term wind maxima. Our results as presented are relatively insensitive to the precise details of this method. For example, a preprint version of this

960 [study \(available via the journal webpage for this article\) used simple estimates of \$u\$ projected directly from individual HLOS measurements rather than this more complicated profile-matching approaches, but produced very similar results for all Figures presented except for a slight reduction in measured absolute wind speeds which this method corrects for.](#)

References

- Baldwin, M. P. and Dunkerton, T. J.: Stratospheric Harbingers of Anomalous Weather Regimes, *Science*, 294, 581–584, 965 <https://doi.org/10.1126/science.1063315>, <https://doi.org/10.1126/science.1063315>, 2001.
- Baldwin, M. P., Ayarzagüena, B., Birner, T., Butchart, N., Butler, A. H., Charlton-Perez, A. J., Domeisen, D. I. V., Garfinkel, C. I., Garny, H., Gerber, E. P., Hegglin, M. I., Langematz, U., and Pedatella, N. M.: Sudden Stratospheric Warmings, *Reviews of Geophysics*, 59, <https://doi.org/10.1029/2020rg000708>, <https://doi.org/10.1029/2020rg000708>, 2021.
- Banyard, T. P., Wright, C. J., Hindley, N. P., Halloran, G., Krisch, I., Kaifler, B., and Hoffmann, L.: Atmospheric Gravity Waves in Aeolus 970 Wind Lidar Observations, <https://doi.org/10.1002/essoar.10506308.1>, <https://doi.org/10.1002/essoar.10506308.1>, 2021.
- Butler, A. H., Sjöberg, J. P., Seidel, D. J., and Rosenlof, K. H.: A sudden stratospheric warming compendium, *Earth System Science Data*, 9, 63–76, <https://doi.org/10.5194/essd-9-63-2017>, <https://doi.org/10.5194/essd-9-63-2017>, 2017.
- Chanin, M., Garnier, A., Hauchecorne, A., and Porteneuve, J.: A Doppler lidar for measuring winds in the middle atmosphere., *Geophysical research letters*, 16, <https://doi.org/10.1029/GL016i011p01273>, 1989.
- 975 Charlton, A. J. and Polvani, L. M.: A New Look at Stratospheric Sudden Warmings. Part I: Climatology and Modeling Benchmarks, *Journal of Climate*, 20, 449–469, <https://doi.org/10.1175/jcli3996.1>, <https://doi.org/10.1175/jcli3996.1>, 2007.
- Charlton-Perez, A. J., Huang, W. T. K., and Lee, S. H.: Impact of sudden stratospheric warmings on United Kingdom mortality, *Atmospheric Science Letters*, <https://doi.org/10.1002/asl.1013>, <https://doi.org/10.1002/asl.1013>, 2020.
- Copernicus Climate Change Service (C3S), .: ERA5: Fifth generation of ECMWF atmospheric reanalyses of the global climate, <https://cds.climate.copernicus.eu/cdsapp#!/home>. 980
- ESA: ALADIN - Atmospheric Laser Doppler Instrument. Working Group Report, ESA SP-1112, p. 45p, 1989.
- ESA: ADM-Aeolus Science Report, ESA SP-1311, p. 121p, 2008.
- France, J. A. and Harvey, V. L.: A climatology of the stratopause in WACCM and the zonally asymmetric elevated stratopause, *Journal of Geophysical Research: Atmospheres*, 118, 2241–2254, <https://doi.org/10.1002/jgrd.50218>, <https://doi.org/10.1002/jgrd.50218>, 2013.
- 985 France, J. A., Harvey, V. L., Randall, C. E., Hitchman, M. H., and Schwartz, M. J.: A climatology of stratopause temperature and height in the polar vortex and anticyclones, *Journal of Geophysical Research: Atmospheres*, 117, n/a–n/a, <https://doi.org/10.1029/2011jd016893>, <https://doi.org/10.1029/2011jd016893>, 2012.
- Gerber, E. P., Martineau, P., Ayarzagüena, B., Barriopedro, D., Bracegirdle, T. J., Butler, A. H., Calvo, N., Hardiman, S. C., Hitchcock, P., Iza, M., Langematz, U., Lu, H., Marshall, G., Orr, A., Palmeiro, F. M., Son, S.-W., and Taguchi, M.: Chapter 6: Extratropical Strato- 990 sphere–troposphere Coupling (submitted), Tech. rep., Stratospheric Reanalysis Intercomparison Report, 2021.
- Hall, R. J., Mitchell, D. M., Seviour, W. J., and Wright, C. J.: Tracking the stratosphere-to-surface impact of Sudden Stratospheric Warmings, *Journal of Geophysical Research: Atmospheres*, <https://doi.org/10.1029/2020jd033881>, <https://doi.org/10.1029/2020jd033881>, 2020.
- Harvey, V. L., Randall, C. E., Goncharenko, L., Becker, E., and France, J.: On the Upward Extension of the Polar Vortices Into the Mesosphere, *Journal of Geophysical Research: Atmospheres*, 123, 9171–9191, <https://doi.org/10.1029/2018jd028815>, <https://doi.org/10.1029/2018jd028815>, 2018. 995
- Harvey, V. L., Randall, C. E., Becker, E., Smith, A. K., Bardeen, C. G., France, J. A., and Goncharenko, L. P.: Evaluation of the Mesospheric Polar Vortices in WACCM, *Journal of Geophysical Research: Atmospheres*, 124, 10 626–10 645, <https://doi.org/10.1029/2019jd030727>, <https://doi.org/10.1029/2019jd030727>, 2019.

- Hersbach, H., Bell, B., Berrisford, P., Hirahara, S., Horányi, A., Muñoz-Sabater, J., Nicolas, J., Peubey, C., Radu, R., Schepers, D., Simmons, A., Soci, C., Abdalla, S., Abellan, X., Balsamo, G., Bechtold, P., Biavati, G., Bidlot, J., Bonavita, M., Chiara, G., Dahlgren, P., Dee, D., Diamantakis, M., Dragani, R., Flemming, J., Forbes, R., Fuentes, M., Geer, A., Haimberger, L., Healy, S., Hogan, R. J., Hólm, E., Janisková, M., Keeley, S., Laloyaux, P., Lopez, P., Lupu, C., Radnoti, G., Rosnay, P., Rozum, I., Vamborg, F., Villaume, S., and Thépaut, J.-N.: The ERA5 global reanalysis, *Quarterly Journal of the Royal Meteorological Society*, 146, 1999–2049, <https://doi.org/10.1002/qj.3803>, <https://doi.org/10.1002/qj.3803>, 2020.
- 1000 Karpechko, A. Y., Hitchcock, P., Peters, D. H. W., and Schneidereit, A.: Predictability of downward propagation of major sudden stratospheric warmings, *Q. J. R. Meteorol. Soc.*, 143, 1459–1470, <https://doi.org/10.1002/qj.3017>, <http://doi.wiley.com/10.1002/qj.3017>, 2017.
- 1005 Kidston, J., Scaife, A. A., Hardiman, S. C., Mitchell, D. M., Butchart, N., Baldwin, M. P., and Gray, L. J.: Stratospheric influence on tropospheric jet streams, storm tracks and surface weather, *Nature Geoscience*, 8, 433–440, <https://doi.org/10.1038/ngeo2424>, <https://doi.org/10.1038/ngeo2424>, 2015.
- 1010 King, A. D., Butler, A. H., Jucker, M., Earl, N. O., and Rudeva, I.: Observed Relationships Between Sudden Stratospheric Warmings and European Climate Extremes, *Journal of Geophysical Research: Atmospheres*, 124, 13 943–13 961, <https://doi.org/10.1029/2019jd030480>, <https://doi.org/10.1029/2019jd030480>, 2019.
- Kolstad, E. W., Breiteig, T., and Scaife, A. A.: The association between stratospheric weak polar vortex events and cold air outbreaks in the Northern Hemisphere, *Quarterly Journal of the Royal Meteorological Society*, 136, 886–893, <https://doi.org/10.1002/qj.620>, <https://doi.org/10.1002/qj.620>, 2010.
- 1015 Kretschmer, M., Cohen, J., Matthias, V., Runge, J., and Coumou, D.: The different stratospheric influence on cold-extremes in Eurasia and North America, *npj Climate and Atmospheric Science*, 1, <https://doi.org/10.1038/s41612-018-0054-4>, <https://doi.org/10.1038/s41612-018-0054-4>, 2018.
- Lawrence, Z. D. and Manney, G. L.: Characterizing Stratospheric Polar Vortex Variability With Computer Vision Techniques, *Journal of Geophysical Research: Atmospheres*, 123, 1510–1535, <https://doi.org/https://doi.org/10.1002/2017JD027556>, 2018.
- 1020 Lawrence, Z. D., Perlwitz, J., Butler, A. H., Manney, G. L., Newman, P. A., Lee, S. H., and Nash, E. R.: The Remarkably Strong Arctic Stratospheric Polar Vortex of Winter 2020: Links to Record-Breaking Arctic Oscillation and Ozone Loss, *Journal of Geophysical Research: Atmospheres*, 125, <https://doi.org/10.1029/2020jd033271>, <https://doi.org/10.1029/2020jd033271>, 2020.
- Livesey, N., Snyder, W. V., Read, W., and Wagner, P.: Retrieval algorithms for the EOS Microwave limb sounder (MLS), *IEEE Transactions on Geoscience and Remote Sensing*, 44, 1144–1155, <https://doi.org/10.1109/tgrs.2006.872327>, <https://doi.org/10.1109/tgrs.2006.872327>, 2006.
- 1025 Livesey, N. J., Read, W. G., Wagner, P. A., Froidevaux, L., Lambert, A., Manney, G. L., Millán Valle, L., Pumphrey, H. C., Santee, M. L., Schwartz, M. J., Wang, S., Fuller, R. A., Jarnot, R. F., Knosp, B. W., and Martinez, E.: Earth Observing System (EOS) Aura Microwave Limb Sounder (MLS) Data Quality and Description, version 4.2, 2015.
- 1030 Lux, O., Lemmerz, C., Weiler, F., Marksteiner, U., Witschas, B., Rahm, S., Geiß, A., and Reitebuch, O.: Intercomparison of wind observations from the European Space Agency's Aeolus satellite mission and the ALADIN Airborne Demonstrator, *Atmospheric Measurement Techniques*, 13, 2075–2097, <https://doi.org/10.5194/amt-13-2075-2020>, <https://doi.org/10.5194/amt-13-2075-2020>, 2020.
- 1035 Manney, G. L., Krüger, K., Pawson, S., Minschwaner, K., Schwartz, M. J., Daffer, W. H., Livesey, N. J., Mlynczak, M. G., Remsberg, E. E., Russell, J. M., and Waters, J. W.: The evolution of the stratopause during the 2006 major warming: Satellite data and assimilated meteorological analyses, *Journal of Geophysical Research*, 113, <https://doi.org/10.1029/2007jd009097>, <https://doi.org/10.1029/2007jd009097>, 2008.

- Manney, G. L., Schwartz, M. J., Krüger, K., Santee, M. L., Pawson, S., Lee, J. N., Daffer, W. H., Fuller, R. A., and Livesey, N. J.: Aura Microwave Limb Sounder observations of dynamics and transport during the record-breaking 2009 Arctic stratospheric major warming, *Geophysical Research Letters*, 36, <https://doi.org/10.1029/2009gl038586>, <https://doi.org/10.1029/2009gl038586>, 2009.
- 1040 Manney, G. L., Lawrence, Z. D., Santee, M. L., Livesey, N. J., Lambert, A., and Pitts, M. C.: Polar processing in a split vortex: Arctic ozone loss in early winter 2012/2013, *Atmospheric Chemistry and Physics*, 15, 5381–5403, <https://doi.org/10.5194/acp-15-5381-2015>, <https://doi.org/10.5194/acp-15-5381-2015>, 2015a.
- Manney, G. L., Lawrence, Z. D., Santee, M. L., Read, W. G., Livesey, N. J., Lambert, A., Froidevaux, L., Pumphrey, H. C., and Schwartz, M. J.: A minor sudden stratospheric warming with a major impact: Transport and polar processing in the 2014/2015 Arctic winter, *Geophysical Research Letters*, 42, 7808–7816, <https://doi.org/10.1002/2015gl065864>, <https://doi.org/10.1002/2015gl065864>, 2015b.
- 1045 Martin, A., Weissmann, M., Reitebuch, O., Rennie, M., Geiß, A., and Cress, A.: Validation of Aeolus winds using radiosonde observations and numerical weather prediction model equivalents, *Atmospheric Measurement Techniques*, 14, 2167–2183, <https://doi.org/10.5194/amt-14-2167-2021>, <https://doi.org/10.5194/amt-14-2167-2021>, 2021.
- Ming, A.: Stratosphere-troposphere coupling in the Earth system: Where next?, *Weather*, 70, 232–233, <https://doi.org/10.1002/wea.2517>, <https://doi.org/10.1002/wea.2517>, 2015.
- 1050 Mitchell, D. M., Gray, L. J., Anstey, J., Baldwin, M. P., and Charlton-Perez, A. J.: The Influence of Stratospheric Vortex Displacements and Splits on Surface Climate, *J. Clim.*, 26, 2668–2682, <https://doi.org/10.1175/JCLI-D-12-00030.1>, <http://journals.ametsoc.org/doi/abs/10.1175/JCLI-D-12-00030.1>, 2013.
- Nakagawa, K. I. and Yamazaki, K.: What kind of stratospheric sudden warming propagates to the troposphere ?, 33, 3–6, <https://doi.org/10.1029/2005GL024784>, 2006.
- 1055 Pedatella, N., Chau, J., Schmidt, H., Goncharenko, L., Stolle, C., Hocke, K., Harvey, V., Funke, B., and Siddiqui, T.: How Sudden Stratospheric Warming Affects the Whole Atmosphere, *Eos*, 99, <https://doi.org/10.1029/2018eo092441>, <https://doi.org/10.1029/2018eo092441>, 2018.
- Polvani, L. M. and Waugh, D. W.: Upward Wave Activity Flux as a Precursor to Extreme Stratospheric Events and Subsequent Anomalous Surface Weather Regimes, *Journal of Climate*, 17, 3548–3554, [https://doi.org/10.1175/1520-0442\(2004\)017<3548:uwafaa>2.0.co;2](https://doi.org/10.1175/1520-0442(2004)017<3548:uwafaa>2.0.co;2), [https://doi.org/10.1175/1520-0442\(2004\)017<3548:uwafaa>2.0.co;2](https://doi.org/10.1175/1520-0442(2004)017<3548:uwafaa>2.0.co;2), 2004.
- 1060 Reitebuch, O.: The spaceborne wind lidar mission ADM-Aeolus., *Atmospheric Physics*, pp. 815–827, https://doi.org/10.1007/978-3-642-30183-4_49, 2012.
- Rennie, M. and Isaksen, L.: The NWP impact of Aeolus Level-2B Winds at ECMWF, <https://doi.org/10.21957/ALIFT7MHR>, <https://www.ecmwf.int/node/19538>, 2020.
- 1065 Rennie, M. P., Isaksen, L., Weiler, F., Kloe, J., Kanitz, T., and Reitebuch, O.: The impact of Aeolus wind retrievals in ECMWF global weather forecasts, *Quarterly Journal of the Royal Meteorological Society*, <https://doi.org/10.1002/qj.4142>, <https://doi.org/10.1002/qj.4142>, 2021.
- Robinson, D. A., Estilow, T. W., and NOAA Climate Data Record Program: NOAA Climate Data Record (CDR) of Northern Hemisphere (NH) Snow Cover Extent (SCE), Version 1, <https://doi.org/10.7289/V5N014G9>, <https://data.nodc.noaa.gov/cgi-bin/iso?id=gov.noaa.ncdc:C00756>, 2014.
- 1070 Safieddine, S., Bouillon, M., Paracho, A.-C., Jumelet, J., Tencé, F., Pazmino, A., Goutail, F., Wespes, C., Bekki, S., Boynard, A., Hadji-Lazaro, J., Coheur, P.-F., Hurtmans, D., and Clerbaux, C.: Antarctic Ozone Enhancement During the 2019 Sudden Stratospheric Warming Event, *Geophysical Research Letters*, 47, <https://doi.org/10.1029/2020gl087810>, <https://doi.org/10.1029/2020gl087810>, 2020.

- Schoeberl, M., Douglass, A., Hilsenrath, E., Bhartia, P., Beer, R., Waters, J., Gunson, M., Froidevaux, L., Gille, J., Barnett, J., Lev-
1075 elt, P., and DeCola, P.: Overview of the EOS aura mission, *IEEE Transactions on Geoscience and Remote Sensing*, 44, 1066–1074,
<https://doi.org/10.1109/tgrs.2005.861950>, <https://doi.org/10.1109/tgrs.2005.861950>, 2006.
- Schwartz, M. J., Lambert, A., Manney, G. L., Read, W. G., Livesey, N. J., Froidevaux, L., Ao, C. O., Bernath, P. F., Boone, C. D., Cofield,
R. E., Daffer, W. H., Drouin, B. J., Fetzer, E. J., Fuller, R. A., Jarnot, R. F., Jiang, J. H., Jiang, Y. B., Knosp, B. W., Krüger, K., Li, J.-L. F.,
Mlynczak, M. G., Pawson, S., Russell, J. M., Santee, M. L., Snyder, W. V., Stek, P. C., Thurstans, R. P., Tompkins, A. M., Wagner, P. A.,
1080 Walker, K. A., Waters, J. W., and Wu, D. L.: Validation of the Aura Microwave Limb Sounder temperature and geopotential height mea-
surements, *Journal of Geophysical Research*, 113, <https://doi.org/10.1029/2007jd008783>, <https://doi.org/10.1029/2007jd008783>, 2008.
- Scott, R. K.: A new class of vacillations of the stratospheric polar vortex, *Quarterly Journal of the Royal Meteorological Society*, 142,
1948–1957, <https://doi.org/10.1002/qj.2788>, <https://doi.org/10.1002/qj.2788>, 2016.
- Seviour, W. J. M., Mitchell, D. M., and Gray, L. J.: A practical method to identify displaced and split stratospheric polar vortex events,
1085 *Geophysical Research Letters*, 40, 5268–5273, <https://doi.org/10.1002/grl.50927>, <https://doi.org/10.1002/grl.50927>, 2013.
- Siskind, D. E., Eckermann, S. D., Coy, L., McCormack, J. P., and Randall, C. E.: On recent interannual variability of the Arctic winter
mesosphere: Implications for tracer descent, *Geophysical Research Letters*, 34, <https://doi.org/10.1029/2007gl029293>, <https://doi.org/10.1029/2007gl029293>, 2007.
- Smith, A. K., Garcia, R. R., Moss, A. C., and Mitchell, N. J.: The Semiannual Oscillation of the Tropical Zonal Wind in the
1090 Middle Atmosphere Derived from Satellite Geopotential Height Retrievals, *Journal of the Atmospheric Sciences*, 74, 2413–2425,
<https://doi.org/10.1175/jas-d-17-0067.1>, <https://doi.org/10.1175/jas-d-17-0067.1>, 2017.
- Stoffelen, A., Pailleux, J., Källén, E., Vaughan, J., Isaksen, L., Flamant, P., Wergen, W., Andersson, E., Schyberg, H., Culoma, A., and
Meynard, R.: The atmospheric dynamics mission for global wind field measurement., *Bulletin of the American Meteorological Society*,
86, <https://doi.org/10.1175/BAMS-86-1-73>, 2005.
- 1095 Stoffelen, A., Benedetti, A., Borde, R., Dabas, A., Flamant, P., Forsythe, M., Hardesty, M., Isaksen, L., Källén, E., Körnich, H., Lee, T.,
Reitebuch, O., Rennie, M., Riishøjgaard, L.-P., Schyberg, H., Straume, A. G., and Vaughan, M.: Wind Profile Satellite Observation
Requirements and Capabilities, *Bulletin of the American Meteorological Society*, 101, E2005–E2021, <https://doi.org/10.1175/bams-d-18-0202.1>, <https://doi.org/10.1175/bams-d-18-0202.1>, 2020.
- Tao, M., Konopka, P., Ploeger, F., Groß, J.-U., Müller, R., Volk, C. M., Walker, K. A., and Riese, M.: Impact of the 2009 major sudden strato-
1100 spheric warming on the composition of the stratosphere, *Atmospheric Chemistry and Physics*, 15, 8695–8715, <https://doi.org/10.5194/acp-15-8695-2015>, <https://doi.org/10.5194/acp-15-8695-2015>, 2015.
- Waters, J., Froidevaux, L., Harwood, R., Jarnot, R., Pickett, H., Read, W., Siegel, P., Cofield, R., Filipiak, M., Flower, D., Holden, J., Lau,
G., Livesey, N., Manney, G., Pumphrey, H., Santee, M., Wu, D., Cuddy, D., Lay, R., Loo, M., Perun, V., Schwartz, M., Stek, P., Thurstans,
R., Boyles, M., Chandra, K., Chavez, M., Chen, G.-S., Chudasama, B., Dodge, R., Fuller, R., Girard, M., Jiang, J., Jiang, Y., Knosp, B.,
1105 LaBelle, R., Lam, J., Lee, K., Miller, D., Oswald, J., Patel, N., Pukala, D., Quintero, O., Scaff, D., Snyder, W. V., Tope, M., Wagner, P.,
and Walch, M.: The Earth observing system microwave limb sounder (EOS MLS) on the aura Satellite, *IEEE Transactions on Geoscience
and Remote Sensing*, 44, 1075–1092, <https://doi.org/10.1109/tgrs.2006.873771>, <https://doi.org/10.1109/tgrs.2006.873771>, 2006.
- Weiler, F., Kanitz, T., Wernham, D., Rennie, M., Huber, D., Schillinger, M., Saint-Pe, O., Bell, R., Parrinello, T., and Reitebuch, O.: Charac-
terization of dark current signal measurements of the ACCDs used on-board the Aeolus satellite, <https://doi.org/10.5194/amt-2020-458>,
1110 <https://doi.org/10.5194/amt-2020-458>, 2020.
- Wright, C.: Detection of stratospheric gravity waves using HIRDLS data, Ph.D. thesis, University of Oxford, 2010.

- Wright, C. J. and Banyard, T. P.: Multidecadal Measurements of UTLS Gravity Waves Derived From Commercial Flight Data, *Journal of Geophysical Research: Atmospheres*, 125, <https://doi.org/10.1029/2020jd033445>, <https://doi.org/10.1029/2020jd033445>, 2020.
- 1115 Wright, C. J. and Hindley, N. P.: How well do stratospheric reanalyses reproduce high-resolution satellite temperature measurements?, *Atmospheric Chemistry and Physics*, 18, 13 703–13 731, <https://doi.org/10.5194/acp-18-13703-2018>, <https://doi.org/10.5194/acp-18-13703-2018>, 2018.
- Wright, C. J., Osprey, S. M., Barnett, J. J., Gray, L. J., and Gille, J. C.: High Resolution Dynamics Limb Sounder measurements of gravity wave activity in the 2006 Arctic stratosphere, *Journal of Geophysical Research*, 115, <https://doi.org/10.1029/2009jd011858>, <https://doi.org/10.1029/2009jd011858>, 2010.
- 1120 Wright, C. J., Hindley, N. P., Moss, A. C., and Mitchell, N. J.: Multi-instrument gravity-wave measurements over Tierra del Fuego and the Drake Passage – Part 1: Potential energies and vertical wavelengths from AIRS, COSMIC, HIRDLS, MLS-Aura, SAAMER, SABER and radiosondes, *Atmospheric Measurement Techniques*, 9, 877–908, <https://doi.org/10.5194/amt-9-877-2016>, <https://doi.org/10.5194/amt-9-877-2016>, 2016.